

Three-Dimensional Integral Boundary Layer Formulation for General Configurations

Mark Drela *

MIT, Cambridge, MA, 02139

A three-dimensional integral boundary layer formulation IBL3 is developed to enable rapid viscous analyses of 3D aerodynamic flows via strongly-coupled viscous/inviscid solution methods. It employs four equations which allow representation of separated flow and crossover profiles, with two additional equations included to model Reynolds stress transport and thus capture turbulence lag effects. In laminar regions the stress-transport equations revert to a form which represents unstable-wave envelope growth, thus making transition prediction an inherent part of the overall formulation.

All six equations have a proper rotation-invariant form which allows solution on arbitrary surface meshes via a finite-element method constructed in a local cartesian basis for each residual stencil. This eliminates the traditional 3D boundary layer curvilinear surface coordinates, and thus sidesteps their inconvenient requirements on geometry smoothness.

The presentation includes the derivation of the integral equations, the formulation of the finite-element solution scheme, and computation of test cases to demonstrate the correctness and accuracy of the overall method. Also presented is the methodology for strong coupling of the integral boundary layer formulation to a number of inviscid-flow solvers.

Nomenclature

| | | | |
|---------------|--------------------------------------|----------------------|---|
| \mathbf{r} | position vector | $\nabla()$ | gradient |
| \mathbf{q} | velocity vector | $\tilde{\nabla}()$ | in-plane gradient ($= \frac{\partial()}{\partial x} \hat{\mathbf{x}} + \frac{\partial()}{\partial z} \hat{\mathbf{z}}$) |
| q | speed ($= \mathbf{q} $) | $\tilde{\mathbf{q}}$ | in-plane velocity vector ($= u \hat{\mathbf{x}} + w \hat{\mathbf{z}}$) |
| ρ | density | $\boldsymbol{\tau}$ | in-plane shear vector ($= \tau_x \hat{\mathbf{x}} + \tau_z \hat{\mathbf{z}}$) |
| p | pressure | $()_i$ | equivalent inviscid flow (EIF) |
| x, y, z | local cartesian-basis coordinates | $()_e$ | edge quantity ($= ()_i$ at y_e) |
| u, v, w | local cartesian-basis velocities | $()_w$ | wall quantity |
| U, W | streamwise, crossflow velocities | $()_1$ | streamwise-axis quantity |
| S, T | streamwise, crossflow shear stresses | $()_2$ | transverse-axis quantity |
| R | normalized density profile | $\hat{()}$ | unit vector |
| \mathcal{D} | dissipation integral | $\bar{()}$ | tensor |

Numerous other quantities, in particular the various integral defects such as m , \mathbf{M} , $\bar{\mathbf{J}}$, etc. and integral thicknesses δ^* , ϕ , θ , θ^* , etc. will be defined later where they first appear.

I. Introduction

A. Background

The viscous/inviscid zonal formulation together with strongly-coupled solution methods has proven to be extremely effective in rapid viscous analyses of 2D aerodynamic flows. Example applications are MSES¹ and XFOIL.² The latter can compute an entire viscous airfoil polar with 20–30 angles of attack, including stall, in only a few seconds. Such speed enables exhaustive aerodynamic design and optimization which would not be practical with much slower computational methods.

*Terry J. Kohler Professor, MIT Department of Aeronautics & Astronautics, AIAA Fellow.

Copyright © 2013 by Mark Drela. Published by the American Institute of Aeronautics and Astronautics, Inc. with permission.

The relative robustness of the strong-coupling method, and also its ability to handle limited flow separation, both stem from its simultaneous solution of the viscous and inviscid equations as a fully-coupled system via a global Newton method. It is highly desirable, if not essential, to retain this simultaneous solution approach for 3D flows. However, using a direct solver for the Newton system is not feasible in 3D, so some type of iterative linear-system solver must be used, such as GMRES with an ILU preconditioner.

A useful halfway approach towards a 3D viscous/inviscid method is to strongly couple a 2D integral boundary layer formulation together with a general 3D inviscid formulation. An example of this is the current TRANAIR code, as described by Bieterman et al,³ where the 2D integral method is extended to include the effects of sweep and lateral divergence, so that it is valid in quasi-2D flow situations such as high aspect ratio swept/tapered wings, and nearly-axisymmetric flows such as fuselages. However, this approach is not valid in fully 3D flows such as wing root and wing tip regions, fuselages and nacelles at significant angles of attack, and wing/fuselage and tail/fuselage intersection regions. For these cases a fully 3D boundary layer method is required.

Traditional finite-difference 3D boundary layer solvers, such as those of Bradshaw and Ferriss⁴ and McLean and Randall,⁵ are fast and effective in the traditional one-way coupled mode where the potential flow is assumed known a priori. However, they require over 100 unknowns to define the boundary layer profiles at each surface point, which would make them relatively slow if they were to be solved simultaneously with the inviscid flow as a two-way strongly coupled system, even with efficient iterative solvers. The demand for computational speed strongly favors methods which require a small number of unknowns to represent the viscous layers. This requirement strongly favors the use of the alternative integral boundary layer formulations for 3D flows.

Numerous 3D integral boundary layer formulations have been developed in the past. Early examples are the methods of Myring,⁶ Bradshaw,⁷ Smith,⁸ Ashill and Smith,⁹ and Swafford and Whitfield.¹⁰ A relatively recent review is given by van Garrel.¹¹ All these methods were formulated in curvilinear coordinates covering the body surface, as were the 3D finite-difference methods. A practical difficulty with such coordinates is their relative intolerance of surface slope discontinuities, which appear as singularities in the surface curvatures and in the corresponding metrics in the equations. Also, if non-orthogonal curvilinear coordinates are employed, as required for complete coverage of a general body shape, the resulting transformed equations become extremely complex. These difficulties of the traditional methods have been sidestepped in the present approach.

B. Present Work

The present IBL3 method is an outgrowth of the earlier works of Mughal¹² and Nishida.¹³ Their major development was to formulate the integral boundary layer equations in finite-element form in local cartesian coordinates defined for each residual. This eliminates the need to construct curvilinear body surface coordinates, and thus largely sidesteps most of the geometry smoothness requirements. It also allows solving the equations on arbitrary triangular or quadrilateral surface grids, and does not require the identification of stagnation points or attachment lines for the application of initial conditions. All these features greatly simplify the application of the 3D integral boundary layer equations to relatively complex surface shapes.

These newer methods still have a few shortcomings of the older methods. Nishida¹³ used a three-equation formulation, which has two streamwise profile modes but only a single crossflow mode. This does not allow representation of crossover profiles which frequently occur in general 3D boundary layers, and thus limits the possible prediction accuracy. An attempt to address the crossover profile problem was made quite early by Stock¹⁴ as an ad-hoc addition to the basic formulation consisting of an additional moment-of-momentum equation. A similar approach was used by Mughal,¹⁵ with the kinetic energy equation being divided into two parts in an ad-hoc manner to provide the additional needed equation. The drawback of these approaches is that they remove in-surface rotational invariance from the equation system, so that the solution depends (hopefully slightly) on the chosen orientation of the two local cartesian axes which are tangent to the surface. The present approach will eliminate any such uncertainties.

Another issue which has received scant attention is the incorporation of a suitable transition prediction method into the integral boundary layer methods. The approach has been to either specify the transition line explicitly, or to use 2D correlations or e^N type methods along strips or streamlines to set the transition location in an ad-hoc loosely coupled manner. This approach is unreliable if transition is triggered by laminar separation, as frequently occurs in low Reynolds number flows. In the “envelope e^N ” formulation used in the 2D MSES and XFOIL codes, the amplification equation which governs the transition location

is solved simultaneously with the inviscid and boundary layer equations, giving a robust overall method for transitional flows. In the present work this strongly-coupled transition prediction formulation is extended and applied to the 3D boundary layer case, so that the transition line is captured in the calculation and does not need to be tracked explicitly.

II. Formulation

A. Defect Formulation

The Equivalent Inviscid Flow (EIF) is an irrotational flow extending down to the wall, which is fictitious inside the shear layer but matches the real flow outside the shear layer, as shown in Figure 1. This enables a defect formulation of the problem, employed originally by leBalleur,¹⁶

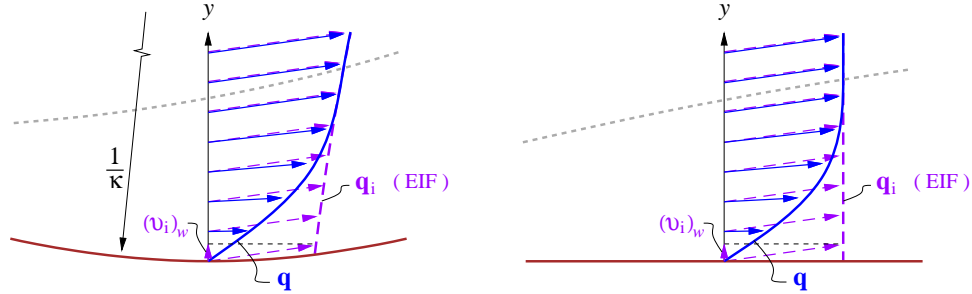


Figure 1. Real viscous flow \mathbf{q} and Equivalent Inviscid Flow \mathbf{q}_i , shown for curved and flat walls.

Consider the integration of a field quantity $f(\mathbf{r})$ over the entire flowfield. This will typically be an equation residual to be driven to zero, or an integrand for an output of interest such as the drag or dissipation. Given the corresponding EIF quantity $f_i(\mathbf{r})$, the volume integral of f can be decomposed into two parts as follows. If the integrand is a divergence, $f = \nabla \cdot \mathbf{f}$, then the same split can be made to the equivalent surface integral.

$$\iiint_{CV} f \, dV = \iiint_{CV} f_i \, dV - \iiint_{DCV} (f_i - f) \, dV \quad (1)$$

$$\text{or} \quad \oiint_{CV} \mathbf{f} \cdot \hat{\mathbf{n}} \, dA = \oiint_{CV} \mathbf{f}_i \cdot \hat{\mathbf{n}} \, dA - \oiint_{DCV} (\mathbf{f}_i - \mathbf{f}) \cdot \hat{\mathbf{n}} \, dA \quad (2)$$

The attractiveness of this decomposition is that f_i corresponds to potential flow and therefore is cheap to evaluate. The remaining defect integrand $f_i - f$ only needs to be evaluated over the much smaller Defect Control Volume (DCV) covering only the viscous parts of the flowfield shown in Figure 2, since it is identically zero elsewhere. This naturally leads to a zonal solution approach, where an inviscid flow method is used to represent the EIF f_i over the entire domain, and a viscous flow method is used to represent the defect $f_i - f$ in the much more compact DCV. It should be noted that such a zonal defect formulation does not inherently depend on the thin shear layer approximations. These enter only when a simplified viscous-flow model is used to more economically solve for the viscous defect.

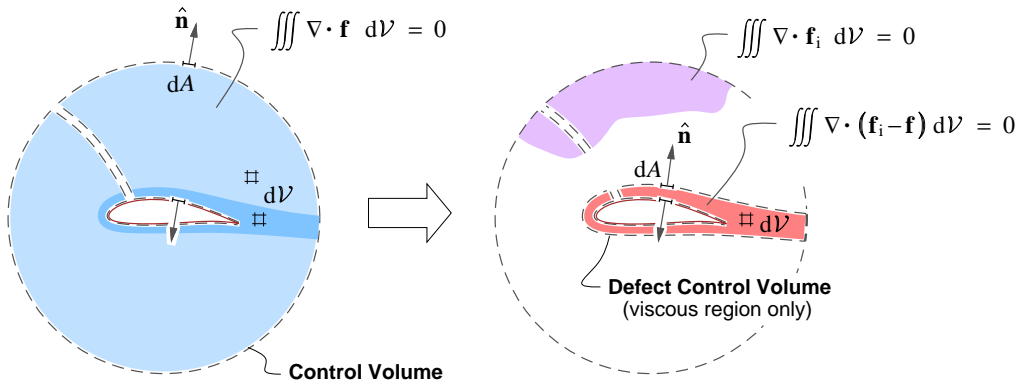


Figure 2. Defect integrand $f_i - f$ needs to be integrated over only the compact Defect Control Volume.

A further decomposition is made by partitioning the DCV into Differential Defect Control Volumes (DDCV), each of which spans the viscous layer as shown in Figure 3. The integral equations treated here will be applied to these DDCV's.

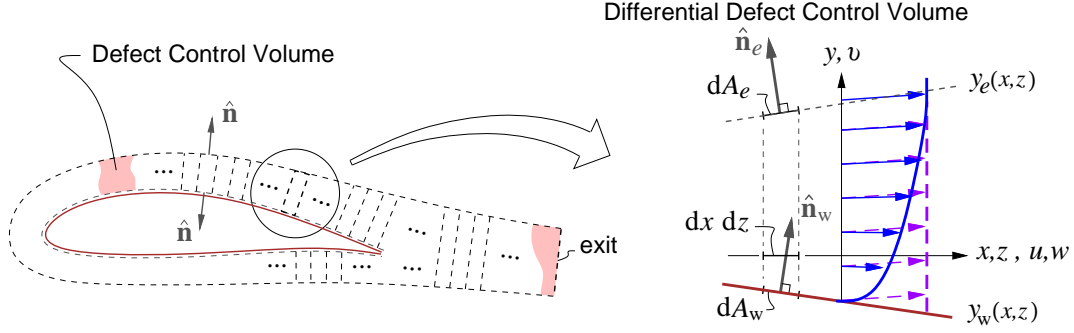


Figure 3. Defect Control Volume as the union of infinitesimal Differential Defect Control Volumes.

The decomposition of the DCV into DDCV's still does not require any thin shear layer approximations. In general, the DDCV's for a curved shear layer would need to vary in width or cross-sectional area along their height. In addition, the EIF velocity profile $\mathbf{q}_i(y)$ would not be constant, as sketched in the curved-wall case in Figure 1. In higher-order boundary layer theory these curvature effects are approximated via terms linear in y . Here, standard boundary layer theory will be employed so that the curvature terms will be neglected. The higher-order treatment may be considered in future work.

B. Global and Local Bases

For computation, all vectors are defined in the usual global cartesian XYZ basis. However, the viscous equation residuals will be constructed in a local xyz basis, where the local coordinates x, y, z and velocity components u, v, w defined at each node, as shown in Figure 4.

$$\begin{aligned} x &= (\mathbf{r} - \mathbf{r}_o) \cdot \hat{\mathbf{x}} & u &= \mathbf{q} \cdot \hat{\mathbf{x}} \\ y &= (\mathbf{r} - \mathbf{r}_o) \cdot \hat{\mathbf{y}} & v &= \mathbf{q} \cdot \hat{\mathbf{y}} \\ z &= (\mathbf{r} - \mathbf{r}_o) \cdot \hat{\mathbf{z}} & w &= \mathbf{q} \cdot \hat{\mathbf{z}} \end{aligned} \quad (3)$$

The local offset \mathbf{r}_o is not essential, but is included to place the xyz origin at a more convenient location, such as a node or element centroid.

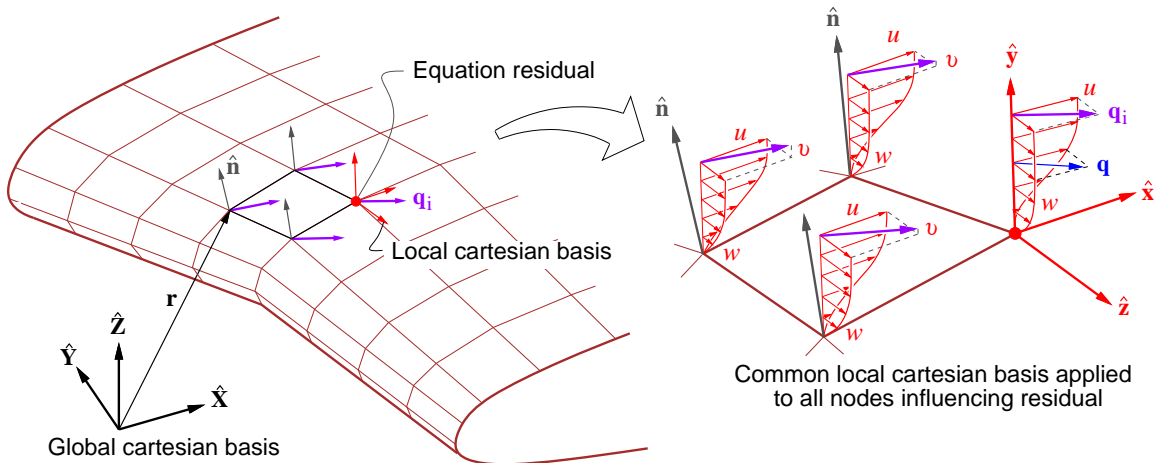


Figure 4. Velocity profiles $\mathbf{q}(y)$ at neighboring cell nodes resolved into u, v, w components in common local xyz basis used for residual construction.

The in-plane velocities u, w are used to define the in-plane flow angle ψ , whose differential will be used

to construct one of the integral boundary layer equations.

$$\psi \equiv \arctan(w/u) \quad (4)$$

$$-\mathbf{q} \times d\mathbf{q} \cdot \hat{\mathbf{y}} = u dw - w du = (u^2 + w^2) d\psi \simeq q^2 d\psi \quad (5)$$

The value of ψ depends on the chosen orientation of the x, z axes, so that rotating them by some angle about the y axis results in a corresponding offset in ψ . However, since the integral boundary layer equations derived later are invariant to such in-plane coordinate rotation, any such offset in ψ has no effect.

C. Gradient and Divergence Relations

The xyz origin can be placed off the surface and inside the shear layer, as shown in Figure 3. The volume integral of a defect divergence over the DDCV is then expanded as follows.

$$\begin{aligned} \iiint \nabla \cdot (\mathbf{f}_i - \mathbf{f}) d\mathcal{V} &= \iint \left[\int_{y_w}^{y_e} \nabla \cdot (\mathbf{f}_i - \mathbf{f}) dy \right] dx dz \\ &= \iint \tilde{\nabla} \cdot \left[\int_{y_w}^{y_e} (\tilde{\mathbf{f}}_i - \tilde{\mathbf{f}}) dy \right] dx dz \\ &\quad + \iint (\mathbf{f}_i - \mathbf{f})_e \cdot \hat{\mathbf{n}}_e dA_e \\ &\quad - \iint (\mathbf{f}_i - \mathbf{f})_w \cdot \hat{\mathbf{n}}_w dA_w = 0 \end{aligned} \quad (6)$$

$$\tilde{\mathbf{f}} = f_x \hat{\mathbf{x}} + f_z \hat{\mathbf{z}} \quad (\text{in-plane flux}) \quad (7)$$

The edge boundary flux term $(\)_e$ vanishes since the defect is zero outside the shear layer by definition.

D. Irrotationality Relations

Since the EIF is irrotational by definition, $\nabla \times \mathbf{q}_i = \mathbf{0}$, the identity

$$\frac{1}{2} \nabla |\mathbf{q}|^2 = \mathbf{q} \cdot \nabla \mathbf{q} + \mathbf{q} \times \nabla \times \mathbf{q}$$

and the inviscid momentum equation give the following relations for the EIF speed and pressure gradients.

$$\begin{aligned} \frac{1}{2} \nabla |\mathbf{q}_i|^2 &= \mathbf{q}_i \cdot \nabla \mathbf{q}_i \\ \nabla p_i &= -\rho_i \frac{\partial \mathbf{q}_i}{\partial t} - \frac{1}{2} \rho_i \nabla |\mathbf{q}_i|^2 \end{aligned} \quad (8)$$

E. Thin Shear Layer Approximations

The EIF viscous stress tensor is assumed to be negligible, $\bar{\bar{\boldsymbol{\tau}}}_i = \bar{\bar{\mathbf{0}}}$. Following the Thin-Layer Navier Stokes approximation, the total defect stress tensor is therefore

$$\left(p_i \bar{\bar{\mathbf{I}}} - \bar{\bar{\boldsymbol{\tau}}}_i \right) - \left(p \bar{\bar{\mathbf{I}}} - \bar{\bar{\boldsymbol{\tau}}} \right) = (p_i - p) \bar{\bar{\mathbf{I}}} + \bar{\bar{\boldsymbol{\tau}}} = \begin{bmatrix} p_i - p & \tau_x & 0 \\ \tau_x & p_i - p & \tau_z \\ 0 & \tau_z & p_i - p \end{bmatrix} \quad (9)$$

where $\tau_x \equiv \tau_{xy}$ and $\tau_z \equiv \tau_{zy}$ are the dominant in-plane shear stress components, and the remaining viscous stress components are assumed negligible. The corresponding defect wall traction vector is

$$\left[(p_i - p) \bar{\bar{\mathbf{I}}} + \bar{\bar{\boldsymbol{\tau}}} \right]_w \cdot \hat{\mathbf{n}}_w = \begin{Bmatrix} (p_i - p) n_x + \tau_x n_y \\ (p_i - p) n_y + \tau_x n_x + \tau_z n_z \\ (p_i - p) n_z + \tau_z n_y \end{Bmatrix}_w \simeq \begin{Bmatrix} \tau_{xw} \\ p_{iw} - p_w \\ \tau_{zw} \end{Bmatrix} \quad (10)$$

where the second approximate expression assumes that the wall-normal vector is nearly along the y axis, or $\hat{\mathbf{n}}_w \simeq \hat{\mathbf{y}}$. However, retaining the exact wall terms does not cause any special difficulties or complications.

The additional approximations $\mathcal{O}\{v/q_i, \kappa(y_e - y_w)\} \ll 1$, give the following standard thin shear layer (or boundary layer) approximations. In a higher-order treatment these would have small correction terms.

$$\begin{aligned} ()_i &\simeq ()_e \simeq ()_{iw} \\ \nabla p &\simeq \nabla p_i \simeq \tilde{\nabla} p_i = -\rho_i \frac{\partial \tilde{\mathbf{q}}_i}{\partial t} - \frac{1}{2} \rho_i \tilde{\nabla} q_i^2 \\ \nabla \cdot \bar{\boldsymbol{\tau}} &\simeq \frac{\partial \boldsymbol{\tau}}{\partial y} = \frac{\partial \tau_x}{\partial y} \hat{\mathbf{x}} + \frac{\partial \tau_z}{\partial y} \hat{\mathbf{z}} \end{aligned} \quad (11)$$

F. Governing Equations

The analysis starts with the usual mass and momentum equations.

$$\frac{\partial \rho}{\partial t} + \nabla \cdot (\rho \mathbf{q}) = 0 \quad (12)$$

$$\rho \frac{\partial \mathbf{q}}{\partial t} + \rho \mathbf{q} \cdot \nabla \mathbf{q} + \nabla p - \nabla \cdot \bar{\boldsymbol{\tau}} = \mathbf{0} \quad (13)$$

Forming $\{[\mathbf{momentum} \text{ (13)}] + \mathbf{q} [\text{mass (12)}]\} \cdot (\hat{\mathbf{x}}, \hat{\mathbf{y}}, \hat{\mathbf{z}})$ puts the momentum equations in divergence form.

$$\frac{\partial(\rho u)}{\partial t} + \nabla \cdot (\rho \mathbf{q} u) + \nabla \cdot (p \hat{\mathbf{x}}) - \nabla \cdot \bar{\boldsymbol{\tau}} \cdot \hat{\mathbf{x}} = 0 \quad (14)$$

$$\frac{\partial(\rho v)}{\partial t} + \nabla \cdot (\rho \mathbf{q} v) + \nabla \cdot (p \hat{\mathbf{y}}) - \nabla \cdot \bar{\boldsymbol{\tau}} \cdot \hat{\mathbf{y}} = 0 \quad (15)$$

$$\frac{\partial(\rho w)}{\partial t} + \nabla \cdot (\rho \mathbf{q} w) + \nabla \cdot (p \hat{\mathbf{z}}) - \nabla \cdot \bar{\boldsymbol{\tau}} \cdot \hat{\mathbf{z}} = 0 \quad (16)$$

Forming $2\mathbf{q} \cdot [\mathbf{momentum} \text{ (13)}] + q^2 [\text{mass (12)}]$ gives the kinetic energy equation in divergence form.

$$\frac{\partial(\rho q^2)}{\partial t} + \nabla \cdot (\rho \mathbf{q} q^2) + 2\mathbf{q} \cdot \nabla p - 2\mathbf{q} \cdot (\nabla \cdot \bar{\boldsymbol{\tau}}) = 0 \quad (17)$$

Forming $-\mathbf{q} \times [\mathbf{momentum} \text{ (13)}] \cdot \hat{\mathbf{y}} + \psi [\text{kinetic energy (17)}]$ gives the lateral-curvature equation.

$$\frac{\partial(\rho q^2 \psi)}{\partial t} + \nabla \cdot (\rho \mathbf{q} q^2 \psi) - \mathbf{q} \times \nabla p \cdot \hat{\mathbf{y}} + \mathbf{q} \times \nabla \cdot \bar{\boldsymbol{\tau}} \cdot \hat{\mathbf{y}} + 2\psi \mathbf{q} \cdot \nabla p - 2\psi \mathbf{q} \cdot (\nabla \cdot \bar{\boldsymbol{\tau}}) = 0 \quad (18)$$

The above equations are also valid for the EIF, except that the viscous stress $\bar{\boldsymbol{\tau}}$ is absent.

G. Integral Defect Definitions

The following integral defects and dissipation integrals will appear when the defect forms of equations (12)–(18) are integrated across the shear layer in the next section.

$$\begin{aligned} m &= \int (\rho_i - \rho) dy && \text{scalar mass defect} \\ e &= \int (\rho_i q_i^2 - \rho q^2) dy && \text{scalar kinetic energy defect} \\ \Pi &= \int (p_i - p) dy && \text{pressure defect} \\ k^\circ &\equiv \int (\psi_i - \psi) \rho q^2 dy && \text{scalar curvature defect} \\ \mathbf{M} &= \int (\rho_i \tilde{\mathbf{q}}_i - \rho \tilde{\mathbf{q}}) dy && \text{mass flux defect} \\ \bar{\mathbf{J}} &= \int (\rho_i \tilde{\mathbf{q}}_i \mathbf{q}_i^T - \rho \tilde{\mathbf{q}} \mathbf{q}_T) dy && \text{momentum flux defect (tensor)} \\ \mathbf{E} &= \int (\rho_i \tilde{\mathbf{q}}_i q_i^2 - \rho \tilde{\mathbf{q}} q^2) dy && \text{kinetic energy flux defect} \\ \mathbf{Q} &= \int (\tilde{\mathbf{q}}_i - \tilde{\mathbf{q}}) dy && \text{volume flux defect} \\ \mathbf{K}^\circ &\equiv \int (\psi_i - \psi) q^2 \rho \tilde{\mathbf{q}} dy && \text{curvature defect flux} \\ \mathbf{Q}^\circ &\equiv \int (\psi_i - \psi) \tilde{\mathbf{q}} dy && \text{curvature defect volume flux} \end{aligned} \quad (19)$$

$$\begin{aligned}
\mathcal{D} &= \int (\bar{\boldsymbol{\tau}} \cdot \nabla) \cdot \mathbf{q} \, dy \simeq \int \boldsymbol{\tau} \cdot \frac{\partial \tilde{\mathbf{q}}}{\partial y} \, dy && \text{dissipation integral} \\
\mathcal{D}^\times &= \int (\bar{\boldsymbol{\tau}} \cdot \nabla) \times \mathbf{q} \cdot \hat{\mathbf{y}} \, dy \simeq \int \boldsymbol{\tau} \times \frac{\partial \tilde{\mathbf{q}}}{\partial y} \cdot \hat{\mathbf{y}} \, dy && \text{shear-anisotropy work integral} \\
\mathcal{D}^\circ &= \int (\bar{\boldsymbol{\tau}} \cdot \nabla) \cdot [(\psi - \psi_i) \mathbf{q}] \, dy \simeq \int \boldsymbol{\tau} \cdot \frac{\partial [(\psi - \psi_i) \tilde{\mathbf{q}}]}{\partial y} \, dy && \text{lateral work integral}
\end{aligned} \tag{20}$$

The approximate forms of the dissipation integrals (20) make use of the thin shear layer approximations.

H. Defect Integral Equations

1. Mass

The mass equation (12) in defect form is integrated across the shear layer and manipulated using relation (6).

$$\begin{aligned}
&\int_{y_w}^{y_e} \left\{ \frac{\partial(\rho_i - \rho)}{\partial t} + \nabla \cdot (\rho_i \mathbf{q}_i - \rho \mathbf{q}) = 0 \right\} dy \\
&\frac{\partial m}{\partial t} + \tilde{\nabla} \cdot \mathbf{M} - (\rho_i \mathbf{q}_i - \rho \mathbf{q})_w \cdot \hat{\mathbf{n}}_w = 0
\end{aligned} \tag{21}$$

The real wall mass flux is dropped for the solid-wall case ($\mathbf{q}_w = \mathbf{0}$), giving the integral mass equation.

$$\boxed{\frac{\partial m}{\partial t} + \tilde{\nabla} \cdot \mathbf{M} - (\rho_i \mathbf{q}_i)_w \cdot \hat{\mathbf{n}}_w = 0} \tag{22}$$

This defines the EIF wall mass flux $(\rho_i \mathbf{q}_i)_w \cdot \hat{\mathbf{n}}_w$ in terms of boundary layer quantities, which is imposed on the inviscid flow in a Viscous/Inviscid coupling scheme. For the case of wall blowing or suction, the $(\rho \mathbf{q})_w$ term would be retained.

2. x, y, z - Momentum

The defect form of the x -momentum equation (14) is integrated across the shear layer, and relation (6) is again used.

$$\begin{aligned}
&\int_{y_w}^{y_e} \left\{ \frac{\partial(\rho_i u_i - \rho u)}{\partial t} + \nabla \cdot (\rho_i \mathbf{q}_i u_i - \rho \mathbf{q} u) + \nabla \cdot (p_i \hat{\mathbf{x}} - p \hat{\mathbf{x}}) + \nabla \cdot (\bar{\boldsymbol{\tau}} \cdot \hat{\mathbf{x}}) = 0 \right\} dy \\
&\frac{\partial M_x}{\partial t} + \tilde{\nabla} \cdot \mathbf{J}^x - (\rho_i \mathbf{q}_i u_i - \rho \mathbf{q} u)_w \cdot \hat{\mathbf{n}}_w + \tilde{\nabla} \Pi + (p_i - p)_w n_{x_w} - \tau_{x_w} = 0
\end{aligned} \tag{23}$$

We now eliminate the EIF wall momentum flux by forming [equation (23)] $- u_{iw}$ [equation (21)] and apply the thin shear layer approximations (11) and the solid-wall boundary condition $\mathbf{q}_w = \mathbf{0}$. The procedure is also repeated for the y and z momentum equations, giving the final integral momentum defect equations.

$$\boxed{\frac{\partial M_x}{\partial t} + \tilde{\nabla} \cdot \mathbf{J}^x - u_{iw} \left(\frac{\partial m}{\partial t} + \tilde{\nabla} \cdot \mathbf{M} \right) - \tau_{x_w} = 0} \tag{24}$$

$$\boxed{\frac{\partial M_y}{\partial t} + \tilde{\nabla} \cdot \mathbf{J}^y - v_{iw} \left(\frac{\partial m}{\partial t} + \tilde{\nabla} \cdot \mathbf{M} \right) + (p - p_i)_w = 0} \tag{25}$$

$$\boxed{\frac{\partial M_z}{\partial t} + \tilde{\nabla} \cdot \mathbf{J}^z - w_{iw} \left(\frac{\partial m}{\partial t} + \tilde{\nabla} \cdot \mathbf{M} \right) - \tau_{z_w} = 0} \tag{26}$$

The present IBL3 formulation will solve only the x and z momentum equations (24) and (26). The y -momentum equation is in effect an expression for the wall pressure defect $p - p_i$, which could be used for higher-order boundary layer theory corrections. These will not be treated here.

3. Kinetic Energy

As with the mass and momentum equations, the defect form of the kinetic energy equation (17) is integrated across the shear layer,

$$\int_{y_w}^{y_e} \left\{ \frac{\partial(\rho_i q_i^2 - \rho q^2)}{\partial t} + \nabla \cdot (\rho_i \mathbf{q}_i q_i^2 - \rho \mathbf{q} q^2) + 2\mathbf{q}_i \cdot \nabla p_i - 2\mathbf{q} \cdot \nabla p + 2\mathbf{q} \cdot (\nabla \cdot \bar{\boldsymbol{\tau}}) = 0 \right\} dy$$

$$\frac{\partial e}{\partial t} + \tilde{\nabla} \cdot \mathbf{E} - (\rho_i \mathbf{q}_i q_i^2 - \rho \mathbf{q} q^2)_w \cdot \hat{\mathbf{n}}_w + 2\mathbf{Q} \cdot \tilde{\nabla} p_i - 2(\mathbf{q} \cdot \boldsymbol{\tau})_w - 2\mathcal{D} = 0 \quad (27)$$

where the shear-work term has been integrated by parts yielding the last two wall-work and dissipation terms in (27). Again we eliminate the wall flux term by forming [equation (27)] - q_{iw}^2 [equation (21)]. Additionally applying the no-slip solid wall condition $\mathbf{q}_w = \mathbf{0}$ and using the EIF relation (8) and the thin shear layer approximations (11) gives the integral kinetic energy defect equation.

$$\boxed{\frac{\partial e}{\partial t} + \tilde{\nabla} \cdot \mathbf{E} - q_{iw}^2 \left(\frac{\partial m}{\partial t} + \tilde{\nabla} \cdot \mathbf{M} \right) - 2\rho_i \mathbf{Q} \cdot \frac{\partial \mathbf{q}_i}{\partial t} - \rho_i \mathbf{Q} \cdot \tilde{\nabla} q_i^2 - 2\mathcal{D} = 0} \quad (28)$$

4. Lateral Curvature

The same defect integration treatment is next applied to the lateral curvature equation (18),

$$\int_{y_w}^{y_e} \left\{ \frac{\partial(\rho_i q_i^2 \psi_i - \rho q^2 \psi)}{\partial t} + \nabla \cdot (\rho_i \mathbf{q}_i q_i^2 \psi_i - \rho \mathbf{q} q^2 \psi) - (\mathbf{q}_i \times \nabla p_i - \mathbf{q} \times \nabla p) \cdot \hat{\mathbf{y}} - \mathbf{q} \times \nabla \cdot \bar{\boldsymbol{\tau}} \cdot \hat{\mathbf{y}} \right. \\ \left. + 2(\psi_i \mathbf{q}_i \cdot \nabla p_i - \psi \mathbf{q} \cdot \nabla p) + 2\psi \mathbf{q} \cdot (\nabla \cdot \bar{\boldsymbol{\tau}}) = 0 \right\} dy$$

which after integration, substitution of the EIF pressure gradient using (8), application of the no-slip condition, and combination with the kinetic energy equation (28), gives the integral lateral-curvature equation.

$$\boxed{\frac{\partial k^\circ}{\partial t} + e \frac{\partial \psi_i}{\partial t} + \tilde{\nabla} \cdot \mathbf{K}^\circ + \mathbf{E} \cdot \tilde{\nabla} \psi_i + \frac{1}{2} \rho_i \mathbf{Q} \times \tilde{\nabla} q_i^2 \cdot \hat{\mathbf{y}} - 2\rho_i \mathbf{Q}^\circ \cdot \frac{\partial \mathbf{q}_i}{\partial t} \\ + \rho_i \mathbf{Q} \times \frac{\partial \mathbf{q}_i}{\partial t} \cdot \hat{\mathbf{y}} - \rho_i \mathbf{Q}^\circ \cdot \tilde{\nabla} q_i^2 + \mathcal{D}^\times - 2\mathcal{D}^\circ = 0} \quad (29)$$

As with all the other previous integral equations, (29) exhibits rotational invariance, in that it does not depend on the orientation of the two in-surface basis vectors $\hat{\mathbf{x}}, \hat{\mathbf{z}}$. In particular, the in-plane angle ψ appears either as a derivative, or as a difference $\psi - \psi_i$ inside the integrals for $k^\circ, \mathbf{K}^\circ, \mathbf{Q}^\circ, \mathcal{D}^\circ$. The cross product terms depend only on the angle between the two vectors involved. Hence, any constant offset in ψ due to xz axis rotation about $\hat{\mathbf{y}}$ is immaterial to equation (29).

5. Turbulent Shear Stress Transport

The outer-layer kinematic Reynolds shear stress $\boldsymbol{\tau}' = \boldsymbol{\tau}/\rho = -\overline{\mathbf{q}'v'}$ is governed by the modeled shear-stress transport equation of Bradshaw,⁷

$$\frac{\partial \boldsymbol{\tau}'}{\partial t} + \mathbf{q} \cdot \nabla \boldsymbol{\tau}' - 2a_1 \left(|\boldsymbol{\tau}'| \frac{\partial \mathbf{q}}{\partial y} - \frac{|\boldsymbol{\tau}'|^{1/2}}{L} \boldsymbol{\tau}' \right) - \frac{\partial \mathbf{f}'_\tau}{\partial y} = \mathbf{0} \quad (30)$$

where $a_1 \equiv |\boldsymbol{\tau}'|/q'^2 = 0.15$ is a Reynolds stress anisotropy ratio which is assumed constant, L is a dissipation length scale, and \mathbf{f}'_τ is a turbulent shear-diffusion flux. Integrating $\int \{\rho [\mathbf{shear} (30)] + \boldsymbol{\tau}' [\mathbf{mass} (12)]\} dy$ across the layer gives the integral shear-stress transport equation in terms of four integral quantities (33).

$$\boxed{\frac{\partial \mathbf{k}^\tau}{\partial t} + \tilde{\nabla} \cdot \bar{\mathbf{K}}^\tau - \mathbf{S}^\tau = \mathbf{0}} \quad (31)$$

$$\mathbf{S}^\tau = 2a_1(\mathcal{P}^\tau - \mathcal{D}^\tau) \quad (\text{turbulent flow}) \quad (32)$$

$$\begin{aligned}
\mathbf{k}^\tau &= \int \rho \boldsymbol{\tau}' dy && \text{shear-stress integral} \\
\bar{\mathbf{K}}^\tau &= \int \rho \boldsymbol{\tau}' \mathbf{q} dy && \text{shear-stress flux integral} \\
\mathcal{P}^\tau &= \int \rho |\boldsymbol{\tau}'| \frac{\partial \mathbf{q}}{\partial y} dy && \text{shear-stress production integral} \\
\mathcal{D}^\tau &= \int \frac{1}{L} \rho |\boldsymbol{\tau}'|^{1/2} \boldsymbol{\tau}' dy && \text{shear-stress dissipation integral}
\end{aligned} \tag{33}$$

The outer-layer dissipation length L is calibrated so that the dissipation integral \mathcal{D} matches the dissipation implied by Clauser's G-beta locus.^{17, 18}

The shear-transport equation (30) models turbulence lags roughly along an outer streamline, and in the 2D case reduces to the lag equation used in MSES¹ and XFOIL,² and is also comparable to the lag equation in Green's lag-entrainment 2D integral boundary layer method.¹⁹ Also significant is that it does not explicitly link the outer shear stress $\boldsymbol{\tau}'$ and the mean-shear direction $\partial \mathbf{q} / \partial y$, so that it allows an effectively non-isotropic eddy viscosity in the outer layer.

6. Tollmien-Schlichting and Cross-Flow Amplitude Evolution

In laminar regions, the shear-stress integral \mathbf{k}^τ is interpreted as the magnitude of the most-amplified Tollmien-Schlichting (TS) and crossflow (CF) wave. This is justified since these instability waves consist of unsteady velocity perturbations \mathbf{q}' which have a nonzero Reynolds stress $\boldsymbol{\tau}'$. In laminar regions the source term in equation (31) is modified to

$$\mathbf{S}^\tau = \frac{q_i |\mathbf{k}^\tau|}{\theta_{11}} \mathbf{f}_N(H_1, Re_\theta) \quad (\text{laminar flow}) \tag{34}$$

where the streamwise component of \mathbf{f}_N is the TS-envelope amplification function used in the XFOIL and MSES envelope- e^N transition prediction formulations. The magnitude of \mathbf{f}_N is nonzero wherever the flow is unstable as determined by the local streamwise shape parameter H and momentum-thickness Reynolds number $Re_\theta = \rho_i q_i \theta_{11} / \mu_i$. At an inflow boundary or stagnation-point cell, the initial condition

$$\mathbf{k}^\tau = \rho_i q_i^2 \theta_{11} \exp(-2N_{\text{crit}}) / C_{\tau_{\text{crit}}} \tag{35}$$

models a low background disturbance level based on the usual N_{crit} transition parameter, and a small nonlinear-breakdown onset parameter $C_{\tau_{\text{crit}}} \simeq 10^{-4}$.

7. Laminar/Turbulent Switching

Which version of the source term \mathbf{S}_τ (laminar or turbulent) is used at any given location is determined by the magnitude of the shear stress coefficients $C_{\tau_{1,2}}$, which scale the outer-layer Reynolds stresses.

$$\begin{aligned}
(C_{\tau_1}^2 + C_{\tau_2}^2)^{1/2} &< C_{\tau_{\text{crit}}} && \rightarrow \text{laminar} \\
(C_{\tau_1}^2 + C_{\tau_2}^2)^{1/2} &> C_{\tau_{\text{crit}}} && \rightarrow \text{turbulent}
\end{aligned}$$

The same criterion determines whether laminar or turbulent profiles are used. These will be defined in the next section. The threshold parameter $C_{\tau_{\text{crit}}}$ represents the fluctuating velocity magnitudes (relative to q_i) which are required to trigger nonlinear breakdown. From the initial condition (35) we see that the precise value of $C_{\tau_{\text{crit}}}$ is not critical. For example, doubling it will have the same effect on transition location as changing N_{crit} from 9 to $9 + \ln 2 = 9.69$, which is well within transition prediction uncertainties.

The overall effect of the present formulation is that C_{τ_1} and C_{τ_2} grow exponentially in the unstable regions, until their magnitude reaches $C_{\tau_{\text{crit}}}$ and thus triggers transition. In the 2D case this formulation is roughly equivalent to the combination of e^N transition prediction method and lag equation which are used in the MSES and XFOIL codes.

I. Consistency with Classical Boundary Layer Theory

With the classical small-curvature BL approximations

$$\begin{aligned}
\mathbf{q}_i &= \mathbf{q}_{i_w} = \text{constant in } y \\
p &= p_i = p_{i_w} = \text{constant in } y
\end{aligned}$$

and assuming steady flow, the present x -momentum equation (24) can be restated as follows.

$$\tilde{\nabla} \cdot (\mathbf{J}^x - u_i \mathbf{M}) + \mathbf{M} \cdot \tilde{\nabla} u_i - \tau_{x_w} = 0 \quad (36)$$

In the 2D case this becomes

$$\frac{d(\mathbf{J} - u_i \mathbf{M})}{dx} + \mathbf{M} \frac{du_i}{dx} - \tau_w = 0 \quad (37)$$

which is the same as the von Karman integral momentum equation

$$\frac{d(\rho_i u_i^2 \theta)}{dx} + \rho_i u_i \delta^* \frac{du_i}{dx} - \tau_w = 0$$

where θ and δ^* are the usual momentum and displacement thicknesses. The present IBL3 integral method therefore contains the classical 2D integral boundary layer formulation as a special case. However, the IBL3 method is somewhat less reliant on the boundary layer approximations.

III. Numerical Solution

This section will describe the process of going from the primary unknowns to the integral defects which appear in the governing equations. Intermediate steps will be viscous velocity and density profile definitions, and integral thickness definitions and calculations. The finite-element discretization method and the calculation of discrete equation residuals will then be described. The procedure for solving the resulting nonlinear system of equations by the Newton method will also be discussed.

A. Primary Viscous Unknowns

Each node on the surface grid has the following six primary viscous unknowns, generically denoted by v_ℓ .

| Unknown | Symbol | Primary function |
|---------|---------------|-------------------------------|
| v_1 | δ | thickness scale |
| v_2 | \mathcal{A} | streamwise profile shape |
| v_3 | \mathcal{B} | crossflow profile shape |
| v_4 | Ψ | profile twist (crossover) |
| v_5 | C_{τ_1} | streamwise outer stress scale |
| v_6 | C_{τ_2} | crossflow outer stress scale |

The components of the Cartesian velocity \mathbf{q}_i are three additional variables, but these are governed by whatever inviscid equation system is used for the EIF, so here the velocities are in effect external parameters.

B. Profile Construction

The velocities within the shear layer are defined using the local streamwise and crossflow basis vectors $\hat{\mathbf{s}}_1, \hat{\mathbf{s}}_2$, where $\hat{\mathbf{s}}_1$ is aligned with the local EIF velocity \mathbf{q}_i , and $\hat{\mathbf{s}}_2$ is orthogonal to both $\hat{\mathbf{s}}_1$ and the wall-normal $\hat{\mathbf{n}}_w$, as shown in Figure 5.

$$\hat{\mathbf{s}}_1 = \frac{\mathbf{q}_i}{q_i} \quad , \quad \hat{\mathbf{s}}_2 = \frac{\hat{\mathbf{s}}_1 \times \hat{\mathbf{n}}_w}{|\hat{\mathbf{s}}_1 \times \hat{\mathbf{n}}_w|} \quad , \quad \hat{\mathbf{n}} = \hat{\mathbf{s}}_2 \times \hat{\mathbf{s}}_1 \quad (38)$$

The local shear layer velocity profile is then defined using the convenient basis velocities \mathbf{q}_1 and \mathbf{q}_2 .

$$\begin{aligned} \mathbf{q}_1 &= q_i \hat{\mathbf{s}}_1 = \mathbf{q}_i \\ \mathbf{q}_2 &= q_i \hat{\mathbf{s}}_2 = \mathbf{q}_i \times \hat{\mathbf{n}} \\ \mathbf{q}(y) &= q_i (U \hat{\mathbf{s}}_1 + W \hat{\mathbf{s}}_2) = U \mathbf{q}_1 + W \mathbf{q}_2 \end{aligned} \quad (39)$$

where $U(y)$ and $W(y)$ are the *streamwise* and *crossflow* normalized velocity profiles. Because $\hat{\mathbf{s}}_1$ is aligned with the EIF velocity, neglecting the remaining vertical velocity component is justified even for a separated

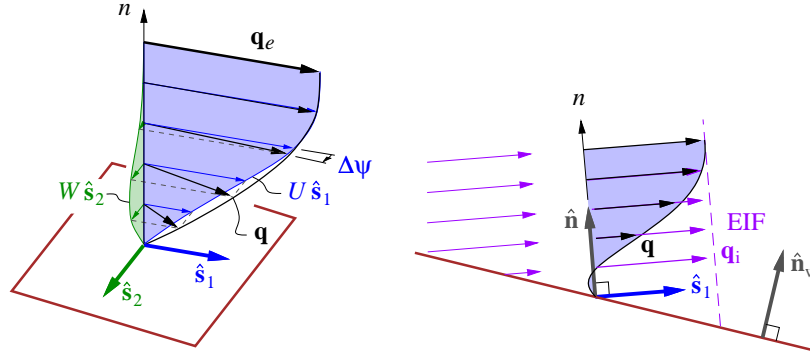


Figure 5. Velocity profile \mathbf{q} formed from streamwise and crossflow profiles U, W along $\hat{\mathbf{s}}_1, \hat{\mathbf{s}}_2$ basis vectors.

boundary layer. This assumption would be less sound if $\hat{\mathbf{s}}_1$ was defined to be tangent to the wall. The lateral angle deviation profile $\Delta\psi$ is defined as

$$\Delta\psi(n) = \psi - \psi_e = \arctan(W/U) \quad (40)$$

The total shear stress profile and the outer-layer kinematic Reynolds shear stress profile are given in terms of the streamwise and crossflow shear stress profiles S, T , and also the outer-layer parts S_o, T_o .

$$\begin{aligned} \boldsymbol{\tau}(y) &= \rho_i q_i^2 (S \hat{\mathbf{s}}_1 + T \hat{\mathbf{s}}_2) = \rho_i q_i (S \mathbf{q}_1 + T \mathbf{q}_2) \\ \boldsymbol{\tau}'(y) &= q_i^2 (S_o \hat{\mathbf{s}}_1 + T_o \hat{\mathbf{s}}_2) = q_i (S_o \mathbf{q}_1 + T_o \mathbf{q}_2) \end{aligned} \quad (41)$$

1. Laminar Profiles

The assumed normalized laminar profiles are a 4-parameter combination of modified Bernstein polynomials $f_{0...3}$, shown in Figure 6, which are functions of the normalized normal coordinate $\eta = y/\delta$.

$$U(y; \mathcal{A}) = \mathcal{A} (1 - 0.6(A-3)\eta^3) f_1(\eta) + f_0(\eta) \quad (42)$$

$$W(y; \delta, \mathcal{B}, \Psi) = \mathcal{B} f_2(\eta) + \Psi f_3(\eta) \quad (43)$$

$$S = \frac{1}{Re_\delta} \frac{\mu}{\mu_i} \frac{dU}{d\eta} \quad (44)$$

$$T = \frac{1}{Re_\delta} \frac{\mu}{\mu_i} \frac{dW}{d\eta} \quad (45)$$

$$\begin{aligned} f_0(\eta) &= 6\eta^2 - 8\eta^3 + 3\eta^4 \\ f_1(\eta) &= \eta - 3\eta^2 + 3\eta^3 - \eta^4 \\ f_2(\eta) &= (\eta - 4\eta^2 + 6\eta^3 - 4\eta^4 + \eta^5) (1 - \eta)^2 \\ f_3(\eta) &= (\eta^2 - 3\eta^3 + 3\eta^4 - \eta^5) (1 - \eta)^2 \end{aligned} \quad (46)$$

The \mathcal{A}, \mathcal{B} parameters specify the direction of the wall streamline, $(U', W')_{\eta=0} = (\mathcal{A}, \mathcal{B})$. A crossover profile is produced by parameter Ψ when its magnitude is comparable to \mathcal{B} , with an opposite sign.

The U profile (42) is a modification of the one used in the old 1-equation Pohlhausen method. A key difference with the present formulation, which is a 2-equation method in 2D (momentum and kinetic energy), is that this eliminates need to explicitly link the parameter \mathcal{A} and the wall skin friction to the local pressure gradient. These are by far the weakest aspects of the Pohlhausen method, but they do not apply here.

2. Turbulent Profiles

The assumed turbulent profiles use the Spalding law of the wall profile $u_s^+(y^+)$ defined in its inverse form $y_s^+(u^+)$, together with the outer wake profile $g_o(\eta)$ of Coles.²⁰ This is extended here to the following 4-parameter 3D profile.

$$U(\eta; \delta, \mathcal{A}, \mathcal{B}, \Psi, q_i) = U_\tau u_s^+(y^+) + K \cos(\Upsilon - \Psi(1 - \eta)^2) g_o(\eta) \quad (47)$$

$$W(\eta; \delta, \mathcal{A}, \mathcal{B}, \Psi, q_i) = W_\tau u_s^+(y^+) - K \sin(\Upsilon - \Psi(1 - \eta)^2) g_o(\eta) \quad (48)$$

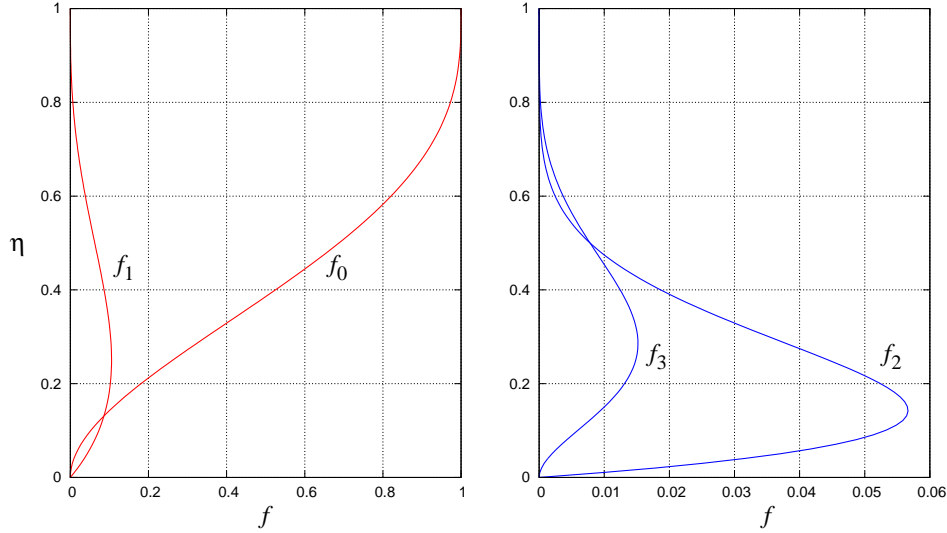


Figure 6. Laminar profile basis functions.

$$S = RU_\tau (U_\tau^2 + W_\tau^2)^{1/2} (1 - g_o) + RC_{\tau_1} K \cos(\Upsilon - \Psi(1 - \eta)^2) g'_o \quad (49)$$

$$T = RW_\tau (U_\tau^2 + W_\tau^2)^{1/2} (1 - g_o) - RC_{\tau_1} K \sin(\Upsilon - \Psi(1 - \eta)^2) g'_o \quad (50)$$

$$\text{where} \quad y_S^+(u^+) = u^+ + e^{-\kappa B} \left[e^{\kappa u^+} - 1 - \kappa u^+ - \frac{1}{2}(\kappa u^+)^2 - \frac{1}{6}(\kappa u^+)^3 \right] \quad (51)$$

$$g_o(\eta) = 3\eta^2 - 2\eta^3 \quad (52)$$

$$K(\delta, \mathcal{A}, \mathcal{B}, q_i) = [(W_\tau u_S^+(\delta^+))^2 + (1 - U_\tau u_S^+(\delta^+))^2]^{1/2} \quad (53)$$

$$\Upsilon(\delta, \mathcal{A}, \mathcal{B}, q_i) = \arctan \frac{W_\tau u_S^+(\delta^+)}{1 - U_\tau u_S^+(\delta^+)} \quad (54)$$

The Spalding profile uses the usual wall coordinate y^+ .

$$y^+ \equiv \frac{\rho_w q_\tau y}{\mu_w} = \eta \delta^+ \quad , \quad \delta^+ \equiv \frac{\rho_w q_\tau \delta}{\mu_w} = Re_\delta^{1/2} \frac{\nu_i}{\nu_w} (\mathcal{A}^2 + \mathcal{B}^2)^{1/4} \quad (55)$$

The wall shear velocities are defined following Bradshaw's⁷ extension of the law of the wall to the 3D case.

$$q_\tau \equiv \left(\frac{|\tau_w|}{\rho_w} \right)^{1/2} = q_i \left(\frac{\nu_w}{\nu_i} \right)^{1/2} \frac{(\mathcal{A}^2 + \mathcal{B}^2)^{1/4}}{Re_\delta^{1/2}} \quad (56)$$

$$U_\tau \equiv \frac{\mathcal{A}}{(\mathcal{A}^2 + \mathcal{B}^2)^{1/4}} \frac{1}{Re_\delta^{1/2}} \quad , \quad W_\tau \equiv \frac{\mathcal{B}}{(\mathcal{A}^2 + \mathcal{B}^2)^{1/4}} \frac{1}{Re_\delta^{1/2}} \quad (57)$$

As in the laminar case, the δ parameter is the overall thickness scale. The two shear velocity components U_τ, W_τ , which are in effect slightly modified versions of the primary parameters \mathcal{A}, \mathcal{B} , give the direction of the wall shear vector τ_w . As in the laminar case, the Ψ parameter provides a non-monotonic “twist” of the overall profile and thus enables the appearance of crossover profiles.

Figure 7 compares the assumed profile for the streamwise component U with five 2D experimental profiles from Simpson et al.²¹ The τ_w parameters were set to their measured values, and δ were determined for a best visual fit to the outer part of the profile.

Figure 8 shows three-dimensional profiles in $W(U)$ polar form measured by Hornung and Joubert²² for a necklace-vortex flow. Station 17 is well inside the necklace vortex, and exhibits strong reverse flow. Clearly this four-parameter profile family is able to capture a wide variety of turbulent flows, including reverse flow and very strong crossflow.

The turbulent shear-stress profiles depend on the outer-layer shear stress coefficients C_{τ_1}, C_{τ_2} , which are two of the six primary variables. They are primarily governed by the turbulent source term \mathbf{S}^τ given by equation (32), and in particular by the dissipation length L in the dissipation integral \mathbf{D}^τ , which is suitably calibrated to obtain the correct results for the G-beta locus flows of Clauser.^{17,18}

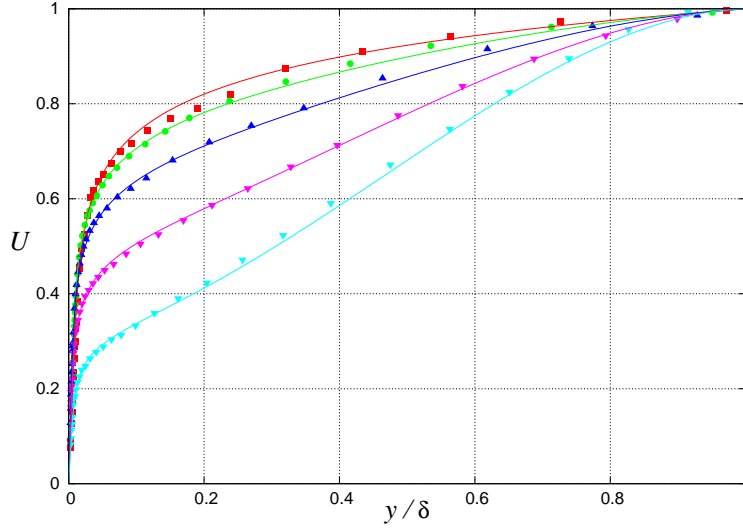


Figure 7. Assumed streamwise profiles (lines) fitted to experimental profiles from Simpson et al.²¹

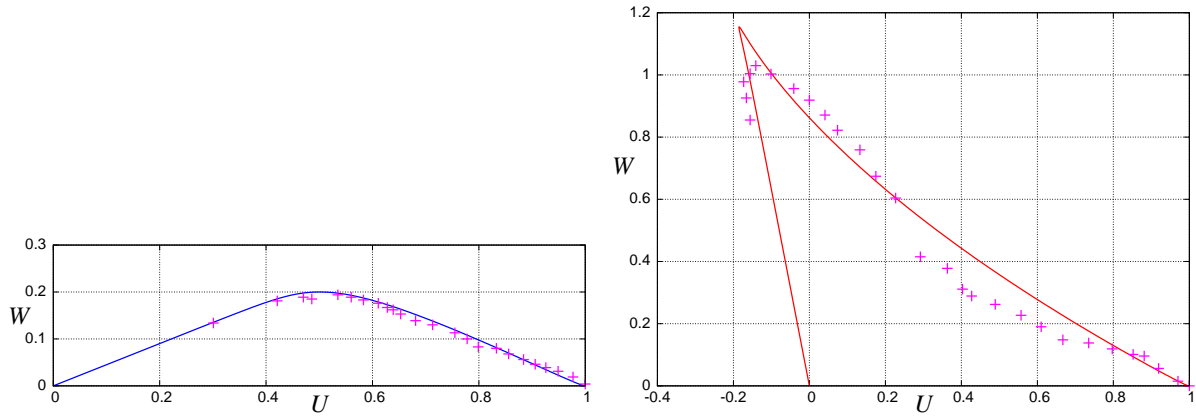


Figure 8. Turbulent polar-profiles fitted to experimental data of a necklace-vortex flow from Hornung and Joubert.²²

3. Density and Viscosity Profiles

With the assumption of constant pressure across the shear layer, the density profile is inversely proportional to the static enthalpy profile. Invoking the Reynolds Analogy, this in turn can be uniquely related to the velocity profiles for the case of unity Prandtl number $Pr = 1$. For nonunity Prandtl numbers, a good approximation is the Crocco-Busemann enthalpy profile,

$$\frac{h}{h_i} = \frac{\rho_i}{\rho} \equiv \frac{1}{R} = 1 + \Delta\mathcal{H}_w (1 - U) + \mathcal{E}' (1 - U^2 - W^2) \quad (58)$$

$$\mathcal{E}' = r \frac{\gamma - 1}{2} M_i^2, \quad \Delta\mathcal{H}_w = \frac{h_w - h_{aw}}{h_i} = \frac{h_w}{h_i} - (1 + \mathcal{E}')$$

where $\Delta\mathcal{H}_w$ is the wall overheat ratio ($= 0$ for an adiabatic wall), \mathcal{E}' is a modified Eckert number, and $r \simeq Pr^{1/2}$ is the temperature recovery factor. This $R(U, W; \Delta\mathcal{H}_w, M_i)$ profile is exact for the case $Pr = 1$, $\tilde{\nabla}p = 0$, and is reasonably accurate otherwise. A more general treatment would be to assume some suitably-parameterized enthalpy profile, and solve the integral thermal defect equation for the additional parameter. The laminar viscosity profile is obtained from the enthalpy profile using Sutherland's law.

$$\frac{\mu}{\mu_i} \equiv \mathcal{M} = \left(\frac{h}{h_i} \right)^{3/2} \frac{1 + h_s/h_i}{h/h_i + h_s/h_i} \quad (59)$$

C. Integral Thickness and Integral Defect Calculation

The assumed $U, W, S, T, R, \mathcal{M}$ profiles enable the definition of the following integral thicknesses.

$$\begin{aligned}
\delta_\rho &= \delta \int (1 - R) \, d\eta & \delta'_1 &= \delta \int (1 - U) \, d\eta \\
\delta_1^* &= \delta \int (1 - RU) \, d\eta & \delta'_2 &= \delta \int (0 - W) \, d\eta \\
\delta_2^* &= \delta \int (0 - RW) \, d\eta & \delta_q &= \phi_{11} + \phi_{22} = \delta \int (1 - R(U^2 + W^2)) \, d\eta \\
\phi_{11} &= \delta \int (1 - RU^2) \, d\eta & \delta_q^\circ &= \delta \int -\Psi (U^2 + W^2) R \, d\eta \\
\phi_{12} = \phi_{21} &= \delta \int (0 - RUW) \, d\eta & \theta_1^\circ &= \delta \int -\Psi (U^2 + W^2) RU \, d\eta \\
\phi_{22} &= \delta \int (0 - RW^2) \, d\eta & \theta_2^\circ &= \delta \int -\Psi (U^2 + W^2) RW \, d\eta \\
\phi_1^* &= \delta \int (1 - RU(U^2 + W^2)) \, d\eta & \delta_1^\circ &= \delta \int -\Psi U \, d\eta \\
\phi_2^* &= \delta \int (0 - RW(U^2 + W^2)) \, d\eta & \delta_2^\circ &= \delta \int -\Psi W \, d\eta
\end{aligned} \tag{60}$$

The various skin friction and dissipation coefficients are similarly defined.

$$\begin{aligned}
C_{f_1} &= 2S(0) & C_{\mathcal{D}} &= \int \left(S \frac{dU}{d\eta} + T \frac{dW}{d\eta} \right) d\eta \\
C_{f_2} &= 2T(0) & C_{\mathcal{D}}^\times &= \int \left(S \frac{dW}{d\eta} - T \frac{dU}{d\eta} \right) d\eta \\
&& C_{\mathcal{D}}^\circ &= \int \left(S \frac{d(\Psi U)}{d\eta} + T \frac{d(\Psi W)}{d\eta} \right) d\eta
\end{aligned} \tag{61}$$

The usual streamwise momentum and kinetic energy thicknesses can also be obtained as follows.

$$\theta_{11} = \delta \int (1 - U) RU \, d\eta = \phi_{11} - \delta_1^* \quad , \quad \theta_1^* = \delta \int (1 - (U^2 + W^2)) RU \, d\eta = \phi_1^* - \delta_1^*$$

In most 2D integral methods the above integrals are pre-computed and implemented as correlation functions. Since in the 3D case the profile parameter space is quite large, making correlations impractical, the integrals are instead evaluated “on the fly” using Gaussian quadrature. The thicknesses and coefficients are then used together with the basis velocities $\mathbf{q}_1, \mathbf{q}_2$ and the edge density ρ_i to compute all the integral defects, the skin friction stress, and the various dissipation integrals. The vectors and tensors at this point are defined in the global cartesian XYZ basis which is used for the \mathbf{q}_1 and \mathbf{q}_2 velocities. For convenience, the EIF subscript $(\cdot)_i$ will be dropped from now on, and all densities, velocities, etc. will be assumed to correspond to the EIF.

$$\begin{aligned}
m &= \rho \delta_\rho \\
e &= \rho q^2 \delta_q \\
k^\circ &= \rho q^2 \delta_q^\circ \\
\mathbf{M} &= \rho (\delta_1^* \mathbf{q}_1 + \delta_2^* \mathbf{q}_2) \\
\bar{\mathbf{J}} &= \rho (\phi_{11} \mathbf{q}_1 \mathbf{q}_1 + \phi_{12} \mathbf{q}_1 \mathbf{q}_2 + \phi_{21} \mathbf{q}_2 \mathbf{q}_1 + \phi_{22} \mathbf{q}_2 \mathbf{q}_2) \\
\mathbf{E} &= \rho q^2 (\phi_1^* \mathbf{q}_1 + \phi_2^* \mathbf{q}_2) \\
\mathbf{K}^\circ &= \rho q^2 (\theta_1^\circ \mathbf{q}_1 + \theta_2^\circ \mathbf{q}_2) \\
\mathbf{Q} &= \delta'_1 \mathbf{q}_1 + \delta'_2 \mathbf{q}_2 \\
\mathbf{Q}^\circ &= \delta_1^\circ \mathbf{q}_1 + \delta_2^\circ \mathbf{q}_2 \\
\boldsymbol{\tau}_w &= \frac{1}{2} \rho q (C_{f_1} \mathbf{q}_1 + C_{f_2} \mathbf{q}_2) \\
\mathcal{D} &= \rho q^3 C_{\mathcal{D}} \\
\mathcal{D}^\times &= \rho q^3 C_{\mathcal{D}}^\times \\
\mathcal{D}^\circ &= \rho q^3 C_{\mathcal{D}}^\circ
\end{aligned} \tag{62}$$

D. Finite Element Solution Method

1. Residual basis vectors and quantities

Each equation residual \mathcal{R}_i associated with a node i must be constructed in a common local basis $\hat{\mathbf{x}}_i, \hat{\mathbf{y}}_i, \hat{\mathbf{z}}_i$, which is applied at each node which contributes to \mathcal{R}_i . Figure 4 shows the four velocity profiles of an element all projected onto a common xyz basis.

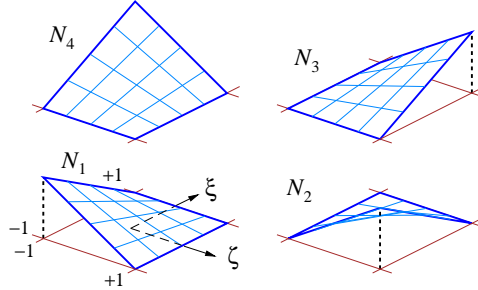
The local boundary layer coordinates x, y, z , velocities u, v, w , and related variables are now defined at all the element's corner nodes j ,

$$\begin{aligned} x_j &= (\mathbf{r}_j - \mathbf{r}_o) \cdot \hat{\mathbf{x}}_i & q_{1x} &= \mathbf{q}_1 \cdot \hat{\mathbf{x}}_i = u_j & q_{2x} &= \mathbf{q}_2 \cdot \hat{\mathbf{x}}_i \\ y_j &= (\mathbf{r}_j - \mathbf{r}_o) \cdot \hat{\mathbf{y}}_i & q_{1y} &= \mathbf{q}_1 \cdot \hat{\mathbf{y}}_i = v_j & q_{2y} &= \mathbf{q}_2 \cdot \hat{\mathbf{y}}_i \\ z_j &= (\mathbf{r}_j - \mathbf{r}_o) \cdot \hat{\mathbf{z}}_i & q_{1z} &= \mathbf{q}_1 \cdot \hat{\mathbf{z}}_i = w_j & q_{2z} &= \mathbf{q}_2 \cdot \hat{\mathbf{z}}_i \end{aligned} \quad (64)$$

These dot products are computed in the global cartesian XYZ basis which is used for all the vectors.

2. Element Interpolation

Velocity components and integral thicknesses are interpolated over the cell via four bilinear basis functions $N_j(\xi, \zeta)$, using the canonical coordinates $-1 \leq \xi \leq +1$, $-1 \leq \zeta \leq +1$ spanning the cell.



$$\begin{aligned} N_1(\xi, \zeta) &= \frac{1}{4}(1 - \zeta)(1 - \xi) \\ N_2(\xi, \zeta) &= \frac{1}{4}(1 + \zeta)(1 - \xi) \\ N_3(\xi, \zeta) &= \frac{1}{4}(1 + \zeta)(1 + \xi) \\ N_4(\xi, \zeta) &= \frac{1}{4}(1 - \zeta)(1 + \xi) \end{aligned}$$

$$\begin{aligned} q_{1x} = u(\xi, \zeta) &= \sum_{j=1}^4 u_j N_j(\xi, \zeta) & \frac{\partial u}{\partial \xi}(\xi, \zeta) &= \sum_{j=1}^4 u_j \frac{\partial N_j}{\partial \xi}(\xi, \zeta) \\ \delta_1^*(\xi, \zeta) &= \sum_{j=1}^4 (\delta_1^*)_j N_j(\xi, \zeta) & \frac{\partial \delta_1^*}{\partial \xi}(\xi, \zeta) &= \sum_{j=1}^4 (\delta_1^*)_j \frac{\partial N_j}{\partial \xi}(\xi, \zeta) \quad \text{etc.} \end{aligned} \quad (65)$$

3. Tangential Gradients

The x, z derivatives are constructed from the x_j, z_j interpolations and their parametric derivatives

$$\begin{aligned} x(\xi, \zeta) &= \sum_{j=1}^4 x_j N_j(\xi, \zeta) & x_\xi &= \sum_{j=1}^4 x_j \frac{\partial N_j}{\partial \xi} & x_\zeta &= \sum_{j=1}^4 x_j \frac{\partial N_j}{\partial \zeta} \\ z(\xi, \zeta) &= \sum_{j=1}^4 z_j N_j(\xi, \zeta) & z_\xi &= \sum_{j=1}^4 z_j \frac{\partial N_j}{\partial \xi} & z_\zeta &= \sum_{j=1}^4 z_j \frac{\partial N_j}{\partial \zeta} \end{aligned} \quad (66)$$

which are then used to form the transformation Jacobian and the reciprocal derivatives $\xi_x, \zeta_x, \xi_z, \zeta_z$. The in-plane gradients in the local xz basis are then obtained via the chain rule.

$$\begin{aligned} \tilde{\nabla} u &= \left(\frac{\partial u}{\partial \xi} \xi_x + \frac{\partial u}{\partial \zeta} \zeta_x \right) \hat{\mathbf{x}} + \left(\frac{\partial u}{\partial \xi} \xi_z + \frac{\partial u}{\partial \zeta} \zeta_z \right) \hat{\mathbf{z}} \\ \tilde{\nabla} \delta_1^* &= \left(\frac{\partial \delta_1^*}{\partial \xi} \xi_x + \frac{\partial \delta_1^*}{\partial \zeta} \zeta_x \right) \hat{\mathbf{x}} + \left(\frac{\partial \delta_1^*}{\partial \xi} \xi_z + \frac{\partial \delta_1^*}{\partial \zeta} \zeta_z \right) \hat{\mathbf{z}} \quad \text{etc.} \end{aligned} \quad (67)$$

4. Time Derivatives

For unsteady-flow cases, the time derivatives are obtained via suitable backwards differencing to give a time-implicit scheme. The simplest is Backward Euler,

$$\begin{aligned} \dot{u}^n &= \frac{1}{\Delta t} [u^n - u^{n-1}] \\ (\dot{\delta}^*)^n &= \frac{1}{\Delta t} [(\delta^*)^n - (\delta^*)^{n-1}] \quad \text{etc.} \end{aligned} \quad (68)$$

where n is the time level. This recovers the steady Newton method in the $\Delta t \rightarrow \infty$ limit, and is best for rapidly driving to steady state. For unsteady cases, a better choice for 2nd-order time accuracy is 3-point backwards differencing.

5. Integral Defect (Flux) Evaluation

The velocities, thicknesses, and their gradients are all evaluated at the Gaussian-quadrature points within each element. The integral defects, which are the fluxes in the governing equations, are then computed at each Gauss point using expressions (62) and (63).

$$\begin{aligned} M_x &= \mathbf{M} \cdot \hat{\mathbf{x}} = \rho \left(\delta_1^* q_{1x} + \delta_2^* q_{2x} \right) \\ P_x^x &= \hat{\mathbf{x}} \cdot \bar{\bar{\mathbf{P}}} \cdot \hat{\mathbf{x}} = \rho_j \left(\theta_{11} q_{1x} q_{1x} + \theta_{12} q_{1x} q_{2x} + \theta_{21} q_{2x} q_{1x} + \theta_{22} q_{2x} q_{2x} \right) \\ P_z^x &= \hat{\mathbf{x}} \cdot \bar{\bar{\mathbf{P}}} \cdot \hat{\mathbf{z}} = \rho_j \left(\theta_{11} q_{1x} q_{1z} + \theta_{12} q_{1x} q_{2z} + \theta_{21} q_{2x} q_{1z} + \theta_{22} q_{2x} q_{2z} \right) \quad \text{etc.} \end{aligned} \quad (69)$$

Their x and z gradients are also used to compute the flux gradients, e.g.

$$\begin{aligned} \tilde{\nabla} M_x &= \tilde{\nabla} \rho \left(\delta_1^* q_{1x} + \delta_2^* q_{2x} \right) \\ &\quad + \rho \left(\tilde{\nabla} \delta_1^* q_{1x} + \delta_1^* \tilde{\nabla} q_{1x} + \tilde{\nabla} \delta_2^* q_{2x} + \delta_2^* \tilde{\nabla} q_{2x} \right) \quad \text{etc.} \end{aligned}$$

With the present bilinear finite element interpolants, these quantities are up to quartic in the element coordinates. The time derivatives of the fluxes are computed in a similar manner.

$$\begin{aligned} \dot{M}_x &= \dot{\rho} \left(\delta_1^* q_{1x} + \delta_2^* q_{2x} \right) \\ &\quad + \rho \left(\dot{\delta}_1^* q_{1x} + \delta_1^* \dot{q}_{1x} + \dot{\delta}_2^* q_{2x} + \delta_2^* \dot{q}_{2x} \right) \quad \text{etc.} \end{aligned}$$

6. Added Numerical Diffusion

Each integral boundary layer equation is stabilized by an added conservative numerical diffusion term formed using the grid cell length matrix $\bar{\bar{\mathbf{h}}}$ and a small diffusion velocity V_ϵ .

$$\frac{\partial M_x}{\partial t} - u \frac{\partial m}{\partial t} + \tilde{\nabla} \cdot \left[\mathbf{J}^x - V_\epsilon \bar{\bar{\mathbf{h}}} \cdot \tilde{\nabla} M_x \right] + u \tilde{\nabla} \cdot \mathbf{M} - \tau_{x_w} = 0 \quad (70)$$

$$\frac{\partial M_z}{\partial t} - w \frac{\partial m}{\partial t} + \tilde{\nabla} \cdot \left[\mathbf{J}^z - V_\epsilon \bar{\bar{\mathbf{h}}} \cdot \tilde{\nabla} M_z \right] + w \tilde{\nabla} \cdot \mathbf{M} - \tau_{z_w} = 0 \quad (71)$$

$$\begin{aligned} &\frac{\partial e}{\partial t} - q^2 \frac{\partial m}{\partial t} - 2\rho \mathbf{Q} \cdot \frac{\partial \mathbf{q}}{\partial t} \\ &\quad + \tilde{\nabla} \cdot \left[\mathbf{E} - V_\epsilon \bar{\bar{\mathbf{h}}} \cdot \tilde{\nabla} e \right] - q^2 \tilde{\nabla} \cdot \mathbf{M} - 2\rho \mathbf{Q} \cdot \tilde{\nabla} q^2 - 2\mathcal{D} = 0 \quad \text{etc.} \end{aligned} \quad (72)$$

$$\begin{aligned} \bar{\bar{\mathbf{h}}} &= \frac{1}{h_\xi} \mathbf{h}_\xi \otimes \mathbf{h}_\xi + \frac{1}{h_\zeta} \mathbf{h}_\zeta \otimes \mathbf{h}_\zeta \\ V_\epsilon &= \epsilon \max_j(q_j) \end{aligned}$$

The $\mathbf{h}_\xi, \mathbf{h}_\zeta$ vectors lie along the surface grid lines at the element in question, with magnitudes h_ξ, h_ζ equal to the grid spacings along those directions. The dissipation level is controlled by the small parameter $\epsilon \simeq 0.001 \dots 0.01$. The integral boundary layer equations are normally hyperbolic, but the diffusion term renders them weakly elliptic, and with a sufficiently large ϵ will smear any steep gradient so that it can be represented on the available local grid spacing. But because the term is conservative, the smearing will not affect the integrated flux of momentum or kinetic energy defect out of the domain (i.e. the total drag or power dissipation), aside from secondary nonlinear errors via the source terms.

This numerical diffusion treatment is analogous to the artificial viscosity or upwinding which must be added to a typical finite-element 2D Euler solver to stabilize it. Such artificial viscosity must be conservative in order to obtain correct local and global conservation.

7. Residual construction

Following the standard Galerkin formulation, a “tent” weighting function $W_i(x(\xi, \zeta), z(\xi, \zeta))$ for each node i residual is defined as the union of individual N_j pieces over the elements which contain node i .

$$W_i = \sum_{\text{elements}} N_j^{\text{element}} = \begin{cases} 1 & \text{at node } j = i \\ 0 & \text{at node } j \neq i \end{cases} \quad (73)$$

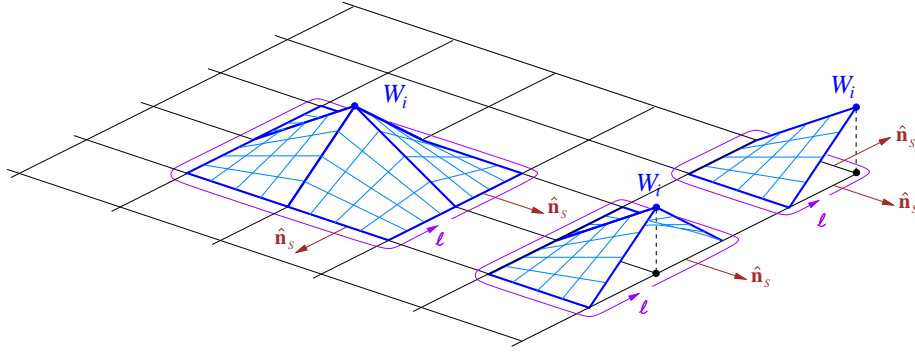


Figure 9. Residual weighting functions for interior, edge, and corner nodes.

Nodes at the edges or corners of the surface grid have partial tent functions as shown in Figure 9.

The residual for each of the six equations integral equations such as (70), for some node i , is defined by integrating each equation with that node's weighting function $W_i(x, z)$.

$$\begin{aligned}\mathcal{R}_i^x &\equiv \iint [\text{equation (70)}] W_i \, dx \, dz \\ &= \oint [-V_\epsilon \bar{\mathbf{h}} \cdot \tilde{\nabla} \mathbf{M}_x] \cdot \hat{\mathbf{n}}_s W_i \, d\ell + \iint [V_\epsilon \bar{\mathbf{h}} \cdot \tilde{\nabla} \mathbf{M}_x] \cdot \tilde{\nabla} W_i \, dx \, dz \\ &\quad + \iint [\nabla \cdot \mathbf{J}^x - u \tilde{\nabla} \cdot \mathbf{M}] W_i \, dx \, dz - \iint \tau_{x_w} W_i \, dx \, dz + \iint [\dot{\mathbf{M}}_x - u \dot{m}] W_i \, dx \, dz\end{aligned}\quad (74)$$

The added-dissipation term has been integrated by parts. The remaining five equations are treated in the same manner to define their corresponding nodal residuals \mathcal{R}_i^z , \mathcal{R}_i^* , \mathcal{R}_i° , $\mathcal{R}_i^{\tau x}$, $\mathcal{R}_i^{\tau z}$. The cell-boundary line integral in (74) and the other residuals are nonzero only for the nodes on the boundary of the domain, typically at the root or tip edge of a wing, and are evaluated using suitable Dirichlet or Neumann boundary conditions. Zero Dirichlet boundary conditions would normally be applied at a leading edge, and zero Neumann conditions would be applied at a side edge where there is no inflow.

All the residual integrals are numerically integrated by Gaussian quadrature by summing over the Gauss points ξ_k, ζ_k , using the transformation coordinates and Jacobian $J = x_\xi z_\zeta - x_\zeta z_\xi$.

$$\iint [\] \, dx \, dz = \iint [\] J \, d\xi \, d\zeta = \sum_k [\]_k J_k w_k \quad (75)$$

8. Viscous-Inviscid Interaction

For the direct problem with prescribed edge velocity \mathbf{q}_i , the boundary layer equations will exhibit the Goldstein singularity²³ if separation is encountered, resulting in solution failure. The singularity is eliminated by allowing the boundary layer to modify the potential flow via the displacement effect, which also enables more accurate drag predictions, and also captures effects such as loss of lift at stall.

The basis of viscous-inviscid interaction models is to impose a boundary condition on the EIF such that the y -component mass flux ρv of the real flow and the EIF become equal for $y > y_e$. This is provided by the integral mass equation (22), which defines the necessary residual to constrain the surface mass flux of the potential flow.

$$\begin{aligned}\mathcal{R}_i^m &\equiv \iint [\text{equation (22)}] W_i \, dx \, dz \\ &= \iint \tilde{\nabla} \cdot \mathbf{M} W_i \, dx \, dz + \iint \dot{m} W_i \, dx \, dz - \iint \left(\rho_i \frac{\partial \phi}{\partial n} \right)_w W_i \, dA_w\end{aligned}\quad (76)$$

The last third term in (76) is typically the wall flux residual which is naturally obtained from a full potential solver which uses the same Galerkin weighted-residual formulation. The first two terms in (76) are therefore the wall-transpiration corrections which must be added to this full potential boundary condition. These are also the terms which produce the two-way coupling between the inviscid and viscous formulations in the overall strongly-coupled method.

IV. Test Cases

A. Torpedo Body over Laminar Plate Flow

In this test case a torpedo body is positioned over a wall, as sketched in Figure 10. The body is simulated very simply with a 3D point source in the nose, which imposes a 3D pressure field on the laminar boundary layer developing on the wall. A wide variety of boundary layer profiles is thus produced on the wall, including strongly-accelerating and nearly-separating profiles, as well as crossover profiles.

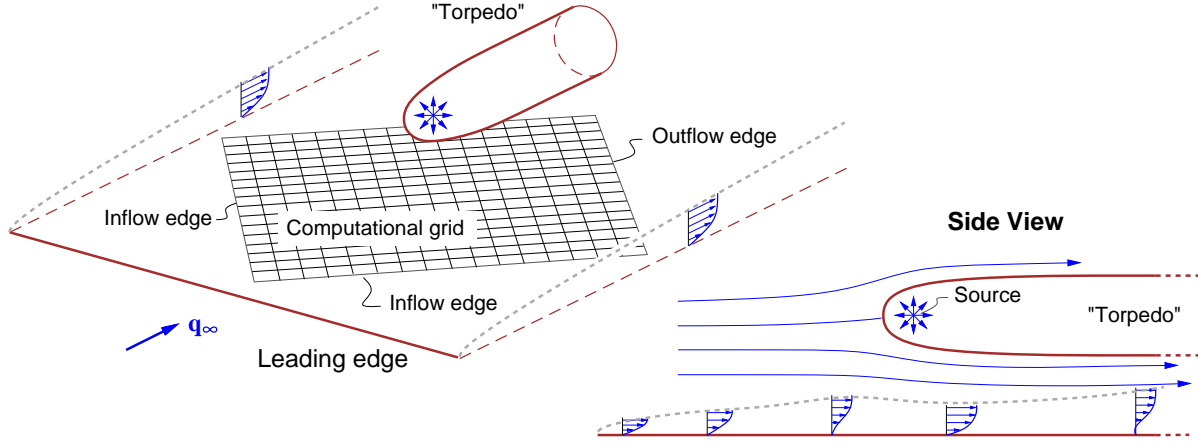


Figure 10. Side view of torpedo body over a wall, imposing 3D pressure gradients on the wall's laminar boundary layer.

A cartesian computational grid is oriented at 45 degrees to the flow, and a Blasius solution assumed to begin at the leading edge is imposed as a boundary condition on the two inflow edges. A classical prescribed-velocity solution computed with a space-marching finite difference method provides an effectively exact reference for evaluation of the present integral method's accuracy for complex laminar flows. Figure 11 compares the streamwise momentum thickness θ_{11} and shape parameter $H_1 = \delta_1^*/\theta_{11}$, crossflow shape parameter $H_2 = \delta_2^*/\theta_{11}$, and the profile-twist parameter Ψ which controls profile crossover. The comparisons are quite acceptable, considering that the integral method requires roughly 100 times fewer unknowns than the finite-difference method. Figure 12 compares the streamwise and laminar profiles at one particular station. The crossover profile is captured quite well.

The boundary layer can be forced to separate by doubling the strength of the point source representing the torpedo. Since a marching solution of the boundary layer equations is no longer possible, these must be solved simultaneously with the potential flow modified by the viscous transpiration velocities. For the simple flat-plate geometry, the potential flow is conveniently represented for by placing a source sheet over each grid cell, whose strength λ is given by the integral mass equation.

$$\rho\lambda_i = 2(\rho\mathbf{q})_w \cdot \hat{\mathbf{n}}_w = 2\tilde{\nabla} \cdot \mathbf{M} \quad (77)$$

The factor of 2 in equation (77) accounts for the image flow under the plate. The EIF velocity at each grid point i is then given via a superposition over all the cell sources.

The primary unknowns of the overall problem are the viscous variables $(\delta \mathcal{A} \mathcal{B} \Psi C_{\tau_1} C_{\tau_2})_i$ at each grid node, and the source strength λ_i at each grid cell. Their governing integral equations, together with the mass equation (77), are solved as a fully-coupled system by the Newton method.

The computed EIF streamlines and wall streamlines (skin friction lines) are shown in Figure 13. The Reynolds number based on the plate length is 10^5 . This demonstrates that the present integral method is capable of capturing closed separations.

B. Unsteady Flow

The present integral method is valid for unsteady flows. Besides enabling nonlinear and linearized unsteady flow calculations, the unsteady terms also provide a convenient and robust means to start a viscous flow calculation. After a reasonable estimate of an inviscid solution is obtained, the no-slip condition is assumed

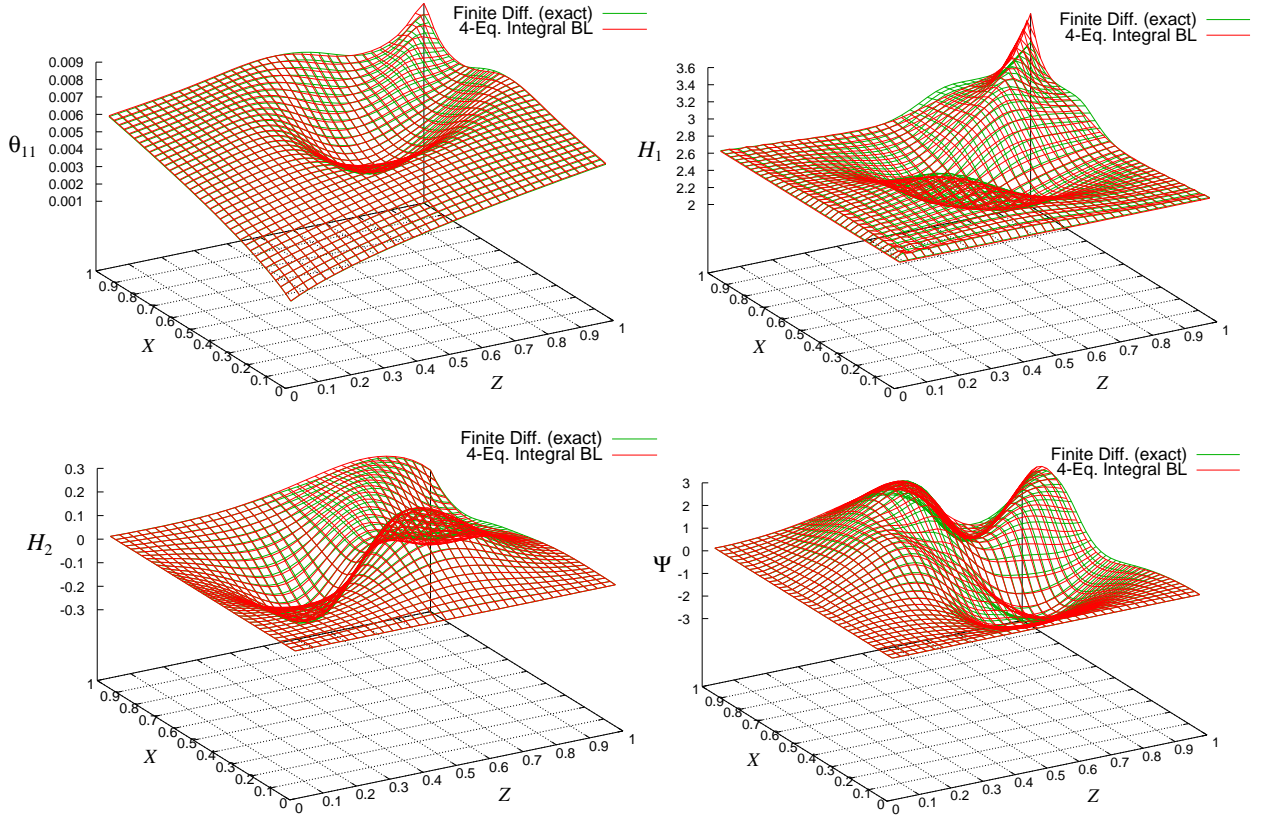


Figure 11. Comparison of parameters for the boundary layer under the torpedo, computed using the present 4-equation integral method and the effectively-exact finite-difference method.

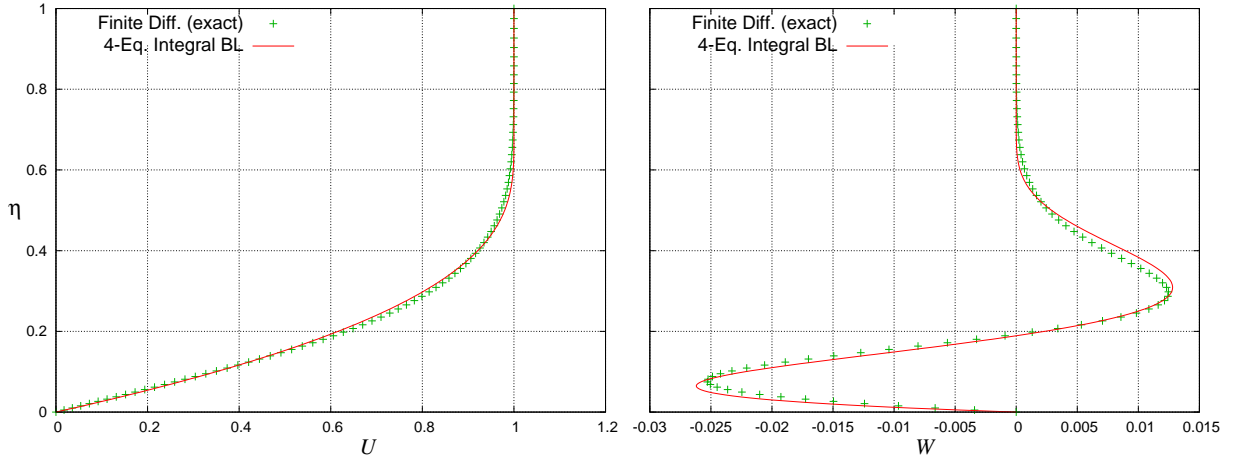


Figure 12. Comparison at one surface location of integral-method profiles and effectively-exact profiles computed using a 3D finite-difference method.

to be suddenly “turned on” everywhere on the surface and wake. After a very short time t_0 , the viscous layer everywhere corresponds to the Rayleigh solution for an impulsively-started wall.

$$U(\eta) = \operatorname{erf}\left(\frac{1}{2}\eta\right) , \quad W(\eta) = 0 \quad \rightarrow \quad \delta \simeq 4.0\sqrt{\nu t_0} , \quad \mathcal{A} \simeq 2.5 , \quad \mathcal{B} = 0 , \quad \Psi = 0 \quad (78)$$

This profile has the streamwise shape parameter $H_1 = \delta_1^*/\theta_{11} \simeq 2.4$, roughly halfway between the flat-plate Blasius flow and the stagnation-point flow. Implicit time-marching steps with backward-Euler differencing can then be performed from this initial solution. The boundary layer thus “grows out of the wall”, and any

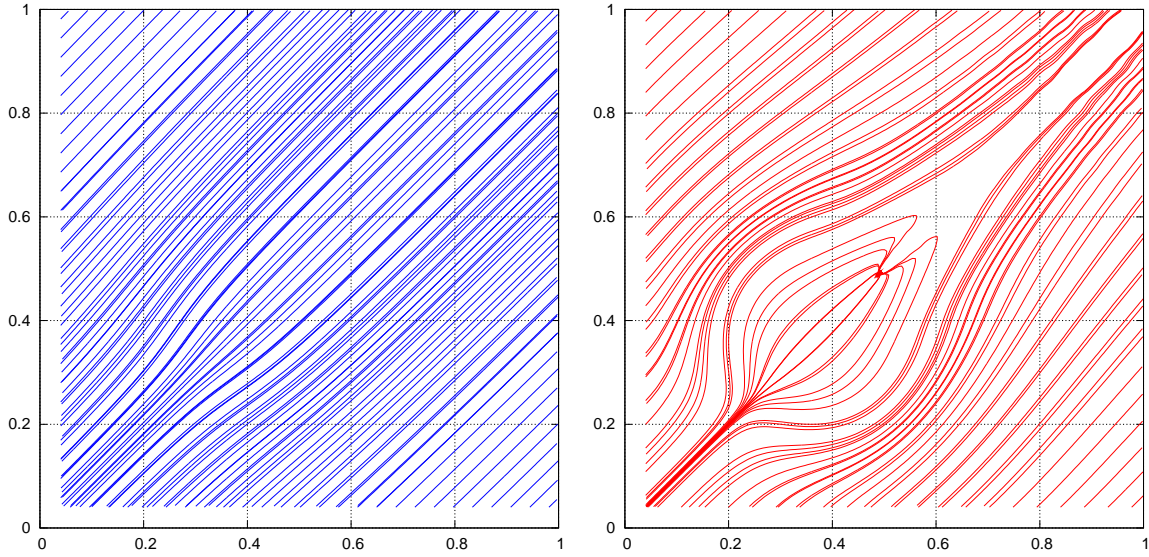


Figure 13. Inviscid and wall streamlines for separated boundary layer under the torpedo.

separations and other features smoothly develop in the process. Progressive increase of the time steps to large levels reverts to Newton convergence to the final steady state. An example of such a calculation for the torpedo case is shown in Figure 14.

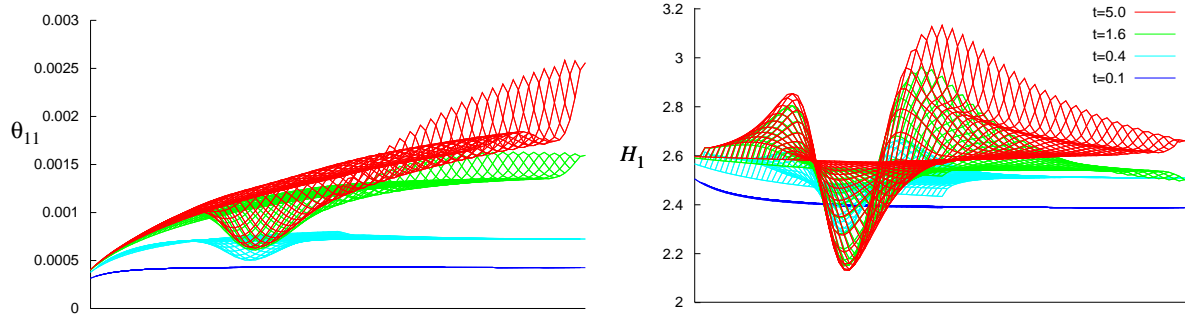


Figure 14. Streamwise momentum thickness and shape parameter time development for the torpedo case, started from a simple Rayleigh solution. The last $t = 5.0$ solution is very nearly at steady state.

C. Low Aspect Ratio Wing with Separation

The ability of the present method to handle realistic 3D geometries is demonstrated by a double-taper wing case, whose surface paneling is shown in Figure 15. The EIF for this case is defined by a low-order panel method with constant doublet strengths μ_i , and constant source-panel strengths

$$\sigma_i = -\mathbf{q}_\infty \cdot \hat{\mathbf{n}}_i + \lambda_i$$

where the additional source-panel contribution λ_i represents the nonzero normal wall EIF velocity due to viscous displacement. The surface velocity is then

$$\mathbf{q}_i(\lambda_j) = \mathbf{q}_{\text{INV}_i} + \mathbf{D}_{ij}\lambda_j \quad (79)$$

where the inviscid-flow velocity $\mathbf{q}_{\text{INV}_i}$ and the influence matrix \mathbf{D}_{ij} are precomputed by the panel method. The computation work required to generate each column of \mathbf{D}_{ij} is comparable to that required for $\mathbf{q}_{\text{INV}_i}$. However, \mathbf{D}_{ij} depends only on the panel and wake geometry, so in practice it needs to be computed only once, and can then be used with any specified magnitude and direction of the freestream velocity \mathbf{q}_∞ .

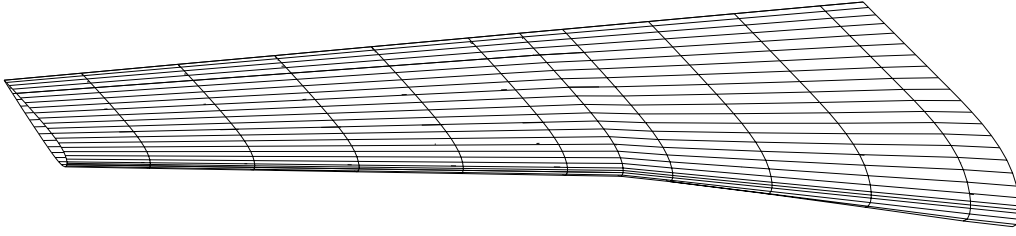


Figure 15. Double-taper wing with 41×12 paneling. Wake 9×12 grid not shown.

For the coupled viscous/inviscid problem, the surface and wake paneling also serves as the boundary layer grid. Each grid node has the six primary viscous unknowns $(\delta \mathcal{A} \mathcal{B} \Psi C_{\tau_1} C_{\tau_2})_i$, governed by the six integral boundary layer equations at all of the interior nodes and at boundary nodes which have an outflow. The center symmetry plane is assumed to be an inviscid wall, so the appropriate boundary conditions there are zero normal fluxes,

$$\mathbf{J}^x \cdot \hat{\mathbf{n}}_s = 0 \quad , \quad \mathbf{J}^z \cdot \hat{\mathbf{n}}_s = 0 \quad , \quad \mathbf{E} \cdot \hat{\mathbf{n}}_s = 0 \quad , \quad \mathbf{K}^\circ \cdot \hat{\mathbf{n}}_s = 0$$

where $\hat{\mathbf{n}}_s$ normal lies in the surface, as shown in Figure 9. At points on the tip airfoil which have an inflow, simple zero spanwise-gradient boundary conditions are applied. The viscous variables and equations are augmented by one source strength λ_i per cell, which is governed by the integral mass equation (77). The EIF node velocities \mathbf{q}_i are explicitly given by (79), and therefore are not additional unknowns.

The 50×12 paneling shown in Figure 15 has 6528 unknowns overall, which is sufficiently small so that the Newton system can be solved by direct elimination. Significantly larger problems will require iterative methods, such as GMRES with a suitable preconditioner. Since the Newton system is reasonably well-conditioned, no special problems are expected here.

Figure 16 shows the computed EIF and wall streamlines on the wing's upper surface for two angles of attack. The separation lines are captured as part of the solution with no special treatment being required. Mathematically these lines are where the characteristics of the hyperbolic equations converge, and hence are analogous to captured shocks in 2D Euler solutions.

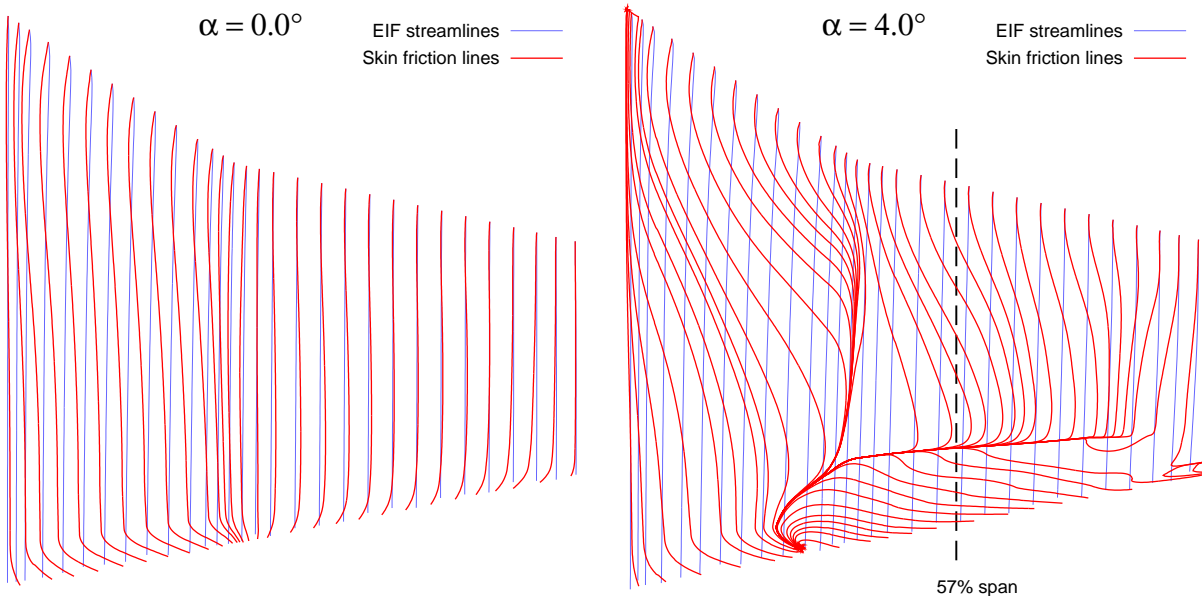


Figure 16. EIF streamlines and wall streamlines on the upper surface of the double-taper wing shown in Figure 15, for two angles of attack. The Reynolds number is 40000, based on the center chord. Pressures at the 57% span location are shown in Figure 17.

The wall streamlines in Figure 16 indicate that the separated flow case $\alpha = 4^\circ$ is roughly two-dimensional over the midspan region. Hence it's useful to compare the solution there with a 2D viscous XFOIL calculation,

at the same local chord Reynolds number $q_\infty c/\nu = 28000$, and with a 2D angle of attack $\alpha = 2.5^\circ$ which nearly matches the local sectional lift coefficient. Figure 17 compares the 3D and 2D pressure distributions. The separation location in the 2D case is at $x/c = 0.79$, which compares reasonably well with the $x/c = 0.76$ separation-line location in the 3D case in Figure 16. The latter has significant lateral-convergence effects in its 3D boundary layer flow, so the separation locations are not expected to match perfectly. Figure 18 compares the streamwise momentum thickness and the N-factor distributions between the 3D case and XFOIL calculations. Given the presence of significant 3D effects, the agreement is reasonable.

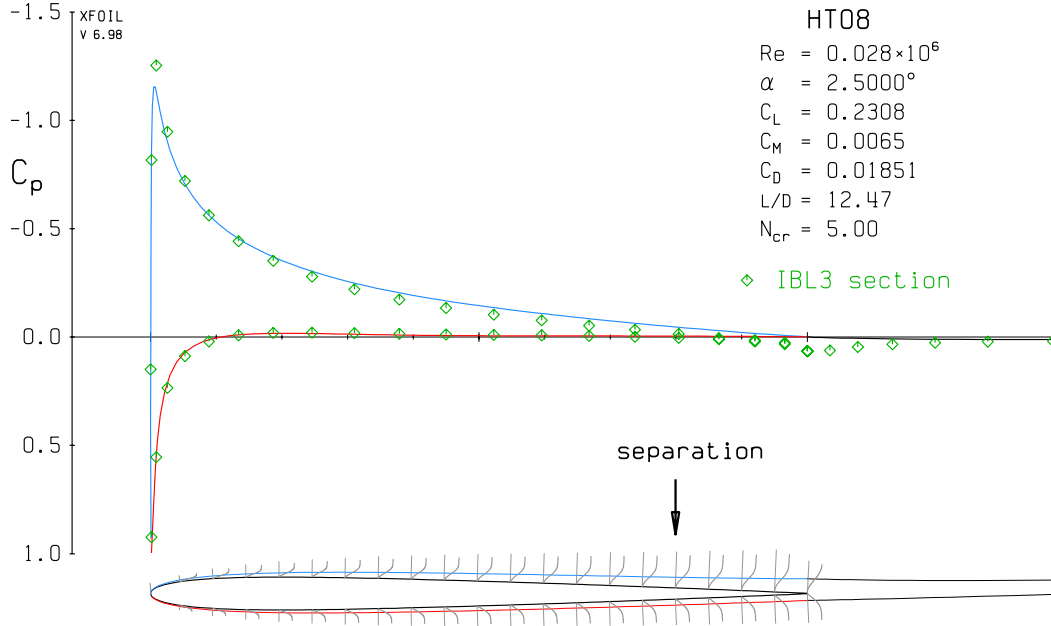


Figure 17. Comparison of a surface pressures from the 3D wing case at 57% span position with 2D results from XFOIL.² The indicated separation location in the XFOIL solution reasonably matches the separation-line location in Figure 16.

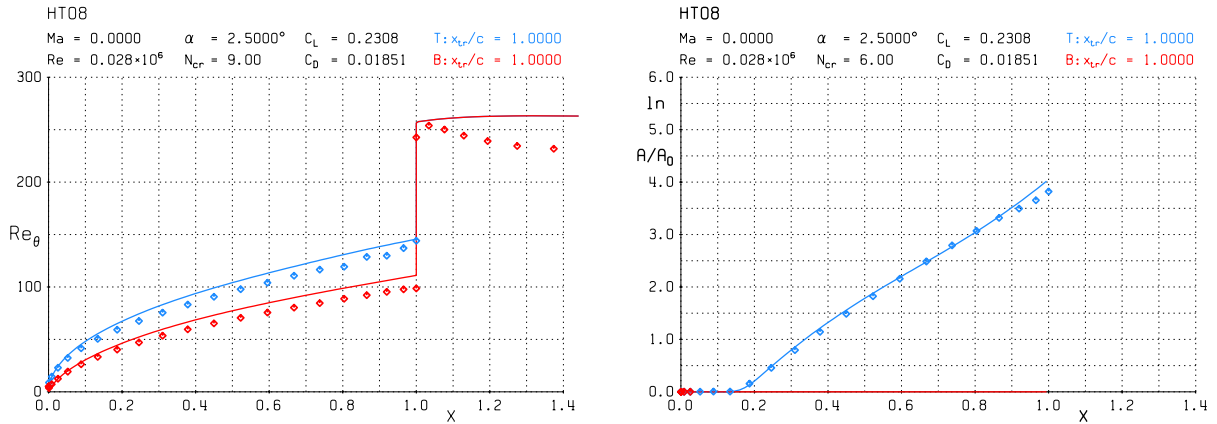


Figure 18. Comparison of streamwise momentum thickness and N-factor at 57% span position (symbols) with 2D results from XFOIL (lines).

As in the torpedo case, the present IBL3 method has the ability to capture separated-flow regions on this wing geometry, as shown in Figure 16. Furthermore, it can also capture stagnation points and attachment lines anywhere within the computational grid, as shown in Figure 19. This makes it a much more “hands-off” viscous flow method than traditional 3D boundary layer solvers, which typically require the identification of an attachment line where the space-marching procedure is started.

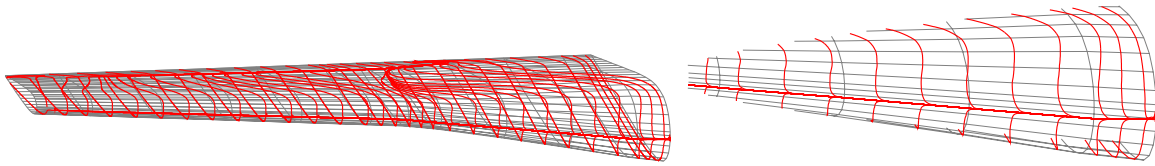


Figure 19. Computed wall streamlines on the leading edge of the double-taper wing at 4° angle of attack. Root region zoom-in is shown on the right. Like the separation lines, the attachment line is also automatically captured within the surface grid.

V. Conclusions

This paper presented a new 3D integral boundary layer formulation IBL3, intended for rapid viscous solutions on general geometries. The test cases presented indicate its effectiveness for fast viscous flow analyses of general 3D aerodynamic flows.

Acknowledgements

This work has been supported by Boeing, with David P. Young and Mori Mani as the technical monitors.

References

- ¹M. Drela and M.B. Giles. Viscous-inviscid analysis of transonic and low Reynolds number airfoils. *AIAA Journal*, 25(10):1347–1355, Oct 1987.
- ²M. Drela. XFOIL: An analysis and design system for low Reynolds number airfoils. In T.J. Mueller, editor, *Low Reynolds Number Aerodynamics*. Springer-Verlag, Jun 1989. Lecture Notes in Engineering, No. 54, <http://raphael.mit.edu/xfoil/>.
- ³M.B. Bieterman, R.G. Melvin, F.T. Johnson, J.E. Bussioletti, D.P. Young, W.P. Huffman, C.L. Hilmes, and M. Drela. Boundary layer coupling in a general configuration full potential code. Technical Report BCSTECH-94-032, Boeing, Aug 1994.
- ⁴P. Bradshaw and D.H. Ferriss. Calculation of boundary-layer development using the turbulent energy equation: Compressible flow on adiabatic walls. *Journal of Fluid Mechanics*, 46:83–110, 1970.
- ⁵J.D. McLean and J.L. Randall. Computer program to calculate three-dimensional boundary layer flows over wings with wall mass transfer. NASA Contractor Report 3123, Boeing Company, Seattle, WA, 1979.
- ⁶D.F. Myring. An integral prediction method for three-dimensional turbulent boundary layers in incompressible flow. Technical Report 32647, Aeronautical Research Council, 1970.
- ⁷P. Bradshaw. Calculation of three-dimensional turbulent boundary layers. *Journal of Fluid Mechanics*, 46:417–445, 1971.
- ⁸P.D. Smith. An integral prediction method for three-dimensional compressible turbulent boundary layers. R & M Report 3739, Aeronautical Research Council, HMSO, London, 1972.
- ⁹P.R. Ashill and P.D. Smith. An integral method for calculating the effects on turbulent boundary-layer development of sweep and taper. *Aeronautical Journal*, Feb:43–54, 1985.
- ¹⁰T.W. Safford and D.L. Whitfield. Time-dependent solution of three-dimensional compressible turbulent integral boundary-layer equations. *AIAA Journal*, 23(7), Jul 1985.
- ¹¹A. van Garrel. Integral boundary layer methods for wind turbine aerodynamics. Technical Report ECN-C-04-004, Netherlands Agency for Energy and the Environment, Dec 2003.
- ¹²B. Mughal and M. Drela. A calculation method for the three-dimensional boundary-layer equations in integral form. AIAA Paper 93-0786, Jan 1993.
- ¹³B. Nishida and M. Drela. Fully simultaneous coupling for three-dimensional viscous/inviscid flows. AIAA-95-1806-CP, June 1995.
- ¹⁴H.W. Stock. Integral methods for the calculation of three-dimensional laminar and turbulent boundary layers. NASA TM-75320, Oct 1977.
- ¹⁵B.H. Mughal. *Integral Methods for Three-Dimensional Boundary Layers*. PhD thesis, MIT, Feb 1998.
- ¹⁶J.C. Le Balleur. Strong matching method for computing transonic viscous flows including wakes and separations. *La Recherche Aerospatiale*, 1981-3:21–45, 1981. English Edition.
- ¹⁷F.H. Clauser. Turbulent boundary layers in adverse pressure gradients. *Journal of the Aeronautical Sciences*, 21(2):91–108, Feb 1954.
- ¹⁸F.H. Clauser. The turbulent boundary layer. *Advances in Applied Mechanics*, 4:1–51, 1956.
- ¹⁹J.E. Green, D.J. Weeks, and J.W.F. Brooman. Prediction of turbulent boundary layers and wakes in compressible flow by a lag-entrainment method. R & M Report 3791, Aeronautical Research Council, HMSO, London, 1977.
- ²⁰D.E. Coles. The law of the wake in the turbulent boundary layer. *Journal of Fluid Mechanics*, 1:193–226, 1956.

²¹R.L. Simpson, Y.T. Chew, and B.G. Shivaprasad. The structure of a separating turbulent boundary layer. part 1. mean flow and reynolds stresses. *Journal of Fluid Mechanics*, 113:23–51, 1981.

²²H.G. Hornung and P.N. Joubert. The mean velocity profile in three-dimensional turbulent boundary layers. *Journal of Fluid Mechanics*, 15:368–384, 1963.

²³S. Goldstein. On laminar boundary layer flow near a position of separation. *Quart. J. or Mech. and Appl. Math.*, pages 1–43, 1948.